Journal of Materials Chemistry A

Capacitive Studies of Electrodeposited PEDOT-maleimide

Journal:	*Journal of Materials Chemistry A*
Manuscript ID	TA-ART-01-2022-000347.R1
Article Type:	Paper
Date Submitted by the Author:	09-Mar-2022
Complete List of Authors:	Wu, Yuhang; University of Delaware, Materials Science and Engineering Nagane, Samadhan; University of Delaware, Materials Science and Engineering Sitarik, Peter; University of Delaware College of Engineering, Materials Science and Engineering Chhatre, Shrirang; University of Delaware, Materials Science and Engineering Lee, Junghyun; University of Delaware Martin, David; University of Delaware, Materials Science and Engineering

ARTICLE

Capacitive Studies of Electrodeposited PEDOT-maleimide

Yuhang Wu,[a] Samadhan S. Nagane,[a] Peter Sitarik,[a] Shrirang Chhatre,[a] Junghyun Lee[a] and David C. Martin*[a,b]

Received 00th January 20xx,
Accepted 00th January 20xx

DOI: 10.1039/x0xx00000x

Here we examined the capacitive behavior of electrodeposited poly(2'-maleimideomethyl-3,4-ethylenedioxythiophene) (PEDOT-maleimide) and compared it to poly(3,4-ethylenedioxythiophene) (PEDOT). According to results of linear cyclic voltammetry (linear CV) and galvanostatic charging/discharging (GCD) in 0.1 M KCl aqueous solution, PEDOT-maleimide presented higher areal specific capacitance, 5.8×10^{-3} Fcm^{-2} at 25 mVs^{-1} and 7.0×10^{-3} Fcm^{-2} at 1.6×10^{-4} Acm^{-2}, while PEDOT exhibited 5.4×10^{-3} Fcm^{-2} at 25 mVs^{-1} and 6.3×10^{-3} Fcm^{-2} at 1.6×10^{-4} Acm^{-2}. Improved cyclic stability of the PEDOT-maleimide was also achieved which correlated with better mechanical properties as revealed by nanoindentation. The effective Young's modulus for PEDOT-maleimide was 4.5 GPa, while it was 1.8 GPa for PEDOT. Roughness studies on surface topographies, determined by atomic force microscopy (AFM) and analyzed by power spectral density (PSD) and root-mean-square (RMS) roughness, revealed that PEDOT-maleimide was rougher than PEDOT at small length scales (below ~1 µm) but smoother at large length scales (above ~1 µm), which was also consistent with complementary observations by scanning electron microscopy (SEM). PEDOT-maleimide showed decreased scattering from the side-to-side (lamellar stacking) ~1.21 nm and ~0.34 nm face-to-face (π-π stacking) signals as confirmed by grazing-incidence wide-angle X-ray scattering (GIWAXS). This change directly made PEDOT-maleimide less conductive than PEDOT, 0.58 *vs.* 3.34 Scm^{-1}. However, the impedance performance across a broad range of frequencies (10^{-1} to 10^{5} Hz) was similar for both PEDOT and PEDOT-maleimide, indicating that both materials remained effective at charge transport. Those results indicate that PEDOT-maleimide is a promising alternative to PEDOT for charge storage applications.

Introduction

Supercapacitors, also known as ultracapacitors, are electrochemical energy storage devices that have been widely investigated for replacing batteries in scenarios requiring fast charging/discharging with little or no decrease of lifetimes.[1–4] They have the ability to store more energy than conventional capacitors and usually perform longer than batteries under fast charging/discharging cycles. Double-layer capacitors and pseudocapacitors are two distinct categories of supercapacitors. Double-layer capacitors operate like conventional capacitors but possess larger active surface areas and shorter separation distances.[5] Unlike double-layer capacitors, pseudocapacitors normally possess far higher specific capacitances (up to 100 times), but at the expense of cyclic stabilities and charging speeds.[6] This is because pseudocapacitors usually rely on fast faradaic redox reactions for charge storage, while double-layer capacitors adopt electrostatic interactions for charge accumulation.[5] Conductive polymers (CPs), such as polyaniline (PANI),[7] polypyrrole (PPy),[8] and poly (3, 4-ethylenedioxythiophene) (PEDOT)[9] have been widely studied as electrode materials for pseudocapacitors. Compared with transition metal oxides such as RuO_2 and MnO_2, CPs' advantages include their low toxicity, processability, and cost. PEDOT is a particularly widely investigated CP that has excellent thermal and moisture stability,[10] tunable mechanical properties,[11] and high conductivity (with highest reported values around 4500 Scm^{-1}).[12] PEDOT has been exploited for its potential use in bioelectronics,[10] light-emitting diodes,[13] and solar cells.[14] However, owing to the high unit mass and low doping level among CPs,[15] the mass-specific capacitance of PEDOT has been reported around 92 Fg^{-1}, which is lower than PPy and PANI (240 and 530 Fg^{-1}, respectively). There are also issues with the cyclic stability of PEDOT due to its relatively low mechanical strength.[16,17] Nevertheless, PEDOT has been found to remain electrically active even after extensive substitution of various side groups on the conjugated backbone, presumably due to its higher molecular rigidity.[18,19]

Different design strategies have been previously applied to enhance the specific capacitances of composite electrode materials involving PEDOT. For example, carbon-based electrodes were used for accommodating electrodeposited PEDOT as well as Ti and electro-spun poly(vinyl alcohol) - graphene oxide (GO) nanofibers.[20–22] Liu et al. achieved higher specific capacitance by precoating traces of nickel-rich oxide on the electrode surfaces.[23] Transition metal oxides,[24,25] GO,[26] carbon nanotubes,[27], or even other CPs have been composited with PEDOT for obtaining higher specific capacitances.[28,29]

[a] *Department of Materials Science and Engineering, University of Delaware, Newark, Delaware 19716, United States.*
[b] *Department of Biomedical Engineering, University of Delaware, Newark, Delaware, 19716, United States. E-mail: milty@udel.edu*
Electronic Supplementary Information (ESI) available: [details of any supplementary information available should be included here]. See DOI: 10.1039/x0xx00000x

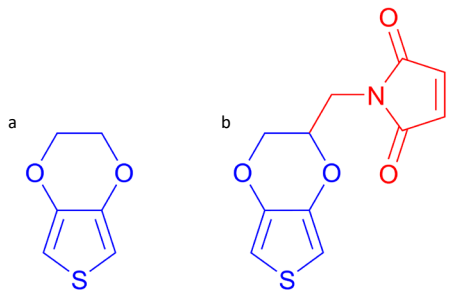

Fig. 1 Chemical structures of (a) EDOT and (b) EDOT-maleimide.

Manipulating geometries and dopants have also shown promise for obtaining higher specific capacitances.[30,31]

In addition to the above-presented methods, chemical modifications are also a potential option for increasing the specific capacitance. Redox groups, like quinones, were attached to PEDOT to achieve better charge storage capability for water-based secondary batteries without compromising the conductivity.[18,32] The substitution of hydrophilic and ionophilic groups like carboxylic acids and hydroxyls onto PEDOT was also reported, but the increments achieved so far have been marginal.[33,34] An extended study was presented by Vermisoglow and colleagues using GO as the virgin material and zwitterions as substituents.[35] However, the impact of other types of functional groups, like maleimides, have yet to be reported. Maleimides are well-known to promote various click reactions,[36] and can also act as redox-active functional groups.[37] We have recently synthesized a maleimide-attached 3,4-ethylenedioxythiophene (EDOT) monomer, 2'-maleimideomethyl-3,4-ethylenedioxythiophene (EDOT-maleimide) (Fig. 1). Here, we investigated the consequence of this maleimide substitution on the charge storage capability of PEDOT-maleimide polymer and compared it with that of PEDOT.[38]

The polymerization potential of EDOT-maleimide as well the potentiodynamic behavior was evaluated and compared with EDOT. Both PEDOT and PEDOT-maleimide films were electrodeposited on gold electrodes at constant voltage for the same total charge densities from their monomer solutions. The capacitive performance of the resulting films was assessed by linear cyclic voltammetry (linear CV), galvanostatic charging/discharging (GCD), and electrochemical impedance spectroscopy (EIS) using a three-electrode setup. Indium tin oxide (ITO) and silicon substrates coated by PEDOT-maleimide and PEDOT were fabricated in staircase CV mode. The samples were examined by a variety of techniques including atomic force microscopy (AFM), scanning electron microscopy (SEM), optical microscopy (OM), X-ray photoelectron spectroscopy (XPS), four-point probe measurements, and UV-visible (UV-vis) absorption spectroscopy. Samples were deposited onto gold/palladium (Au/Pd) alloy coated silicon substrates for grazing-incidence wide-angle X-ray scattering (GIWAXS).

Experimental

Materials

3,4-ethylenedioxythiophene (EDOT) and lithium perchlorate ($LiClO_4$) were acquired from Sigma-Aldrich and used as received. Phosphate buffered saline (PBS), potassium chloride (KCl), potassium hydroxide (KOH), and acetonitrile were procured from Thermo Fisher Scientific and used as received. Deionized water (DI water) was prepared by a Milli-Q Reference water purification system in our lab. Screen-printed electrodes (SPEs) of types C223BT and C220BT integrated with 1.6- and 4-mm diameter gold circle working electrodes, respectively, surrounded by the gold counter and silver pseudoreference (-0.133 V *vs.* Ag/AgCl) electrodes, where the electric contacts were also made out of silver, were purchased from Metrohm. If not otherwise specified, potentials presented in this work were all referred to the silver pseudoreference electrode. Indium tin oxide (ITO) coated glass substrates of 0.6×2.5 cm^2 were obtained from Delta Technologies. Silicon wafers were acquired from University Wafers with a diameter of 100 mm.

2'-maleimideomethyl-3,4-ethylenedioxythiophene (EDOT-maleimide) was synthesized following our published synthetic route.[38] The proton NMR peaks were: 1H NMR (400 MHz, $CDCl_3$): δ=6.77 (s, 2H), 6.33 (d, 2H), 4.39 (d, 1H), 4.21 (d, 1H), 3.98-3.88 (m, 2H), 3.73 (dd, 1H), 13C NMR: δ=170.2, 141.0, 134.3, 100.2, 70.9, 66.1, 37.7 ppm.

Electrodepositions

A Metrohm Autolab PGSTAT128N potentiostat/galvanostat was used for the electrodepositions throughout this work. All electrodepositions were carried out at room temperature and pressure in a Faraday cage. When PEDOT and PEDOT-maleimide were electrodeposited on SPEs, 0.01 M EDOT and EDOT-maleimide acetonitrile solution with 0.02 M LiClO4 was prepared, respectively. Around 50 µl of this solution was syringed to fully cover all electrodes for electrodeposition. Staircase CV was operated from -1.0 to 1.3 V for 5 cycles at 100 mVs^{-1} with a step size of 2.44×10^{-3} V on C223BT for studying the potentiodynamic polymerization of EDOT and EDOT-maleimide. Staircase linear sweep voltammetry (LSV) from 1.0 to 1.3 V at 5 and 50 mVs^{-1} with the same step size as the staircase CV was also performed on C223BT to determine the polymerization potential which was defined as the x-axis intercept of the tangent line passing through the inflection point after the current rose. According to the LSV results, the polymerization potentials of EDOT and EDOT-maleimide were determined respectively as 1.12 and 1.13 V at 5 mVs^{-1}. Considering that the polymerization started earlier than what was deduced from LSV for the potentiostatic mode then the potential chosen for potentiostatic deposition was 1.10 V in the rest of this paper if not otherwise specified. Supercapacitive performance was evaluated on PEDOT and PEDOT-maleimide films electrodeposited on C223BT in potentiostatic mode consuming a charge density of 7.7×10^{-2} Ccm^{-2}, which is equivalent to an effective thickness of around one micrometer of electrodeposited PEDOT film based on an empirical equation previously deduced in our lab.[39] The cyclic stability evaluation was accomplished on C220BT samples made at the same charge density. PEDOT and PEDOT-maleimide coated ITO samples,

electrodeposited by staircase CV from -0.5 to 1.5 V in 0.01 M monomer and 0.1 M $LiClO_4$ acetonitrile solution passing 0.11 Ccm^{-2} charges, gave intact and even films of around 0.60 cm^2 area. These samples were subjected to AFM, SEM, XPS, UV-vis, four-point probe, and OM characterizations.[40] Silicon substrates of around 1 cm^2 area, cut from a silicon wafer, were sputter-coated by a Denton Vacuum Desk IV Sputter employing Au/Pd alloy for 200 s, and the ensuing electrodepositions were carried out under the same conditions as ITO samples. GIWAXS on the PEDOT and PEDOT-maleimide coated silicon substrates was performed. A glass well was used to contain reaction solutions and the whole C220BT served as counter and reference electrodes with working electrode disconnected. ITO or coated silicon substrates were used as the working electrode for their electrodepositions. All samples electrodeposited for further characterization were rinsed consecutively with excess acetonitrile and DI water for removing any unreacted monomers left on electrodes and were dried and stored at room temperature under nitrogen atmosphere.

Characterization of Morphology, Surface Chemistry, Optical Properties, and Electrical Conductivity

ITO samples were used throughout all characterizations covered in this section except for GIWAXS which was done on silicon substrates. UV-vis spectra from 400 to 1400 nm were recorded on a Shimadzu UV-3600 UV-vis-NIR spectrophotometer. OM was accomplished with a Nikon Eclipse LVPOL100. Samples were sputter-coated by the Au/Pd alloy via Denton Vacuum Desk IV Sputter for ca. 45 s for SEM. SEM was performed on a JEOL JSM- 7400F at an accelerating voltage of 3 kV. XPS spectra were acquired through a Thermo Fisher K-alpha+ spectrometer installed with a monochromator and a 128 channel CCD detector plate. The sample surface was illuminated with monochromatic Al Kα X-rays (1486.7 eV) and the spot size was an ellipse with a semi-major axis of 400 µm. Initial XPS survey scans were taken at pass energy of 100 eV with a step size of 1 eV. High-resolution XPS spectra were taken at a pass energy of 20 eV with a step size of 0.1 eV and ten scans were collected. Two areas on each sample were scanned in both modes. GIWAXS was operated on Xeuss 2.0 HR SAXS/WAXS. Cu Kα with a wavelength of 1.54 Å was the X-ray source. The sample to detector distance was 100 mm and the incidence angle of the probing X-ray was 0.2°. A Lucas 302 resistivity stand coupled with a Keithley 2400 source meter was used for the sheet resistance assessment. The sample thickness was estimated from cross-section images taken on an Auriga 60 CrossBeam SEM at an accelerating voltage of 3 kV using the tilting function at 65°. For each cross-section image, three data points were collected for representing the corresponding sample.

Mechanical and Roughness Characterization

Given the rough working electrode of SPEs, ITO substrates were selected for the mechanical characterization considering the sensitivity of the nanoindentation method. An RTESPA-300 tip installed on a Bruker Multimode Atomic Force Microscope was used for data collection, and NanoScope Analysis and Gwyddion software were used for data analysis. The resonant frequency and the spring constant of this type of tip were 300 kHz and 40 Nm^{-1}, respectively. Due to the potential for abrasion of tips during characterization, the tip radius was calibrated before and after the characterization on a TiO_2 sample with well-defined pyramid shapes on the surface. After analyzing the scanned images of several 2×2 μm^2 areas on TiO_2, the average tip end radius was determined to be 15 nm. To estimate the mechanical properties, indentation depths of 10 nm on the sample surface were used for all measurements. 20×20 points with 50 nm intervals on 1 μm^2 square area were mapped for the data collection. The effective Young's modulus was extracted from the force-extension curve of each indentation applying a Linearized Hertzian model and the R^2 larger than 0.9 was set as the bar to validate the model fitting. In general, two 1 μm^2 square areas from each sample, i.e., 800 points, were indented, and effective Young's moduli from three samples were averaged over the resulting dataset and analyzed statistically.

To quantify the difference in surface roughness observed through SEM, topographies of PEDOT and PEDOT-maleimide coated ITO samples were collected across four different length scales: 1, 5, 10, and 15 µm. Images taken at 15×15 μm^2 contained 768×768 data points, 10×10 μm^2 contained 512×512 data points, 5×5 μm^2 contained 256×256 data points, and 1×1 μm^2 contained 64×64 data points. The contact mode and the same AFM tips were chosen for collecting topographies. The power spectral density (PSD) of 15×15 μm^2 scans were determined with NanoScope Analysis software and the corresponding fractal dimensions (FD) were obtained by fitting the increasing region of PSD linearly. Besides, the root-mean-square (RMS) roughness, as well as the effective surface areas of topographies at all probed length scales, were also evaluated.

Electrochemical Characterization

Electrochemical characterizations were carried out on C223BT type electrodes with 0.1 M KCl as the supporting electrolyte. Linear CV was recorded on a Solartron Analytical Modulab potentiostat/galvanostat from 0 to 0.5 V under various scan rates. GCD, EIS, self-discharging, and leakage current measurements were conducted on a Metrohm Autolab PGSTAT128N potentiostat/galvanostat. GCD was examined under different charging/discharging rates within the same voltage window as linear CV. The frequency range for EIS characterization was from 10^{-1} to 10^5 Hz with an amplitude of 10 mV and the background voltage at 0 V. Before characterizing the self-discharging and the leakage current, the whole cell was discharged until the potential reached 0 V. Self-discharging studies were implemented as follows. In the beginning, the cell was charged at 1.6×10^{-4} Acm^{-2} current density until the cell potential hit 0.5 V. Then the current was shut, and the open-circuit potential of the whole cell was constantly monitored before the discharging rate fell off and reached a preset cutoff, of $dE/dt < 10^{-6}$ Vs^{-1}. Concerning the leakage current, 0.5 V constant potential was kept on the cell and the current evolution for the next hour was monitored. The undulating

current at the end of the curve was identified as the leakage current, the minimum current used to keep the cell on charge. C220BT samples were immersed into 1×PBS solution for studying cyclic stabilities through executing staircase CV from -0.8 to 0.8 V for 500 cycles at 100 mVs^{-1}. Changes in their EIS before and after staircase CV were indicative of cyclic stability. All measurements mentioned above were done on three individual samples for statistical significance and reproducibility.

Results and discussion

Electrodepositions of EDOT and EDOT-maleimide

To study the impact of the maleimide substitution on the monomer polymerization potential, staircase LSVs were carried out on EDOT and EDOT-maleimide at two different scan rates, 5 and 50 mVs^{-1}. Due to the unchanged step size, the interval time at 5 mVs^{-1} was ten times more than 50 mVs^{-1}, therefore we observed that the current surged earlier at 5 mVs^{-1}, as shown in Fig. 2. This behavior was presumably related to the kinetics of polymerization. At 5 mVs^{-1}, each voltage step lasted longer allowing monomers to re-establish non-bonded interactions as well as offering enough time for diffusion from the bulk solution to the surface. Thus, the current response of polymerization at lower scan rates emerged earlier than at higher scan rates. The polymerization potential in this work was defined as the x-axis intercept of the tangent line passing the inflection point after the current went up, i.e. the maximum of the first derivative or the intercept with the x-axis of the second derivative. Inflection points of all curves are marked as the green dots in Fig. 2 and the tangent line of EDOT scanned at 5 mVs^{-1} is given as an example. It was clear that EDOT possessed lower polymerization potentials than EDOT-maleimide at both scan rates, which indicated that the substitution added extra steric pressure on the arrangement of polymer units. However, the difference in polymerization potential between EDOT and EDOT-maleimide was smaller at 5 mVs^{-1} than at 50 mVs^{-1}. This basically meant that EDOT-maleimide benefitted more from the longer interval

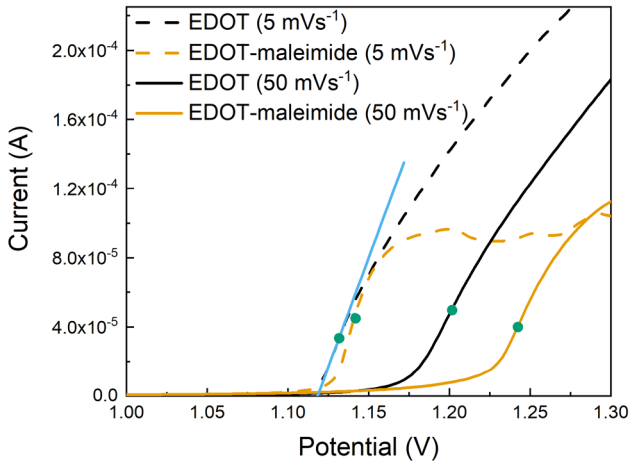

Fig. 2 Staircase LSVs of EDOT and EDOT-maleimide at 5 and 50 mVs^{-1}. Green dots denote the inflection points, and the cyan line is the tangent line of EDOT (5 mVs^{-1}).

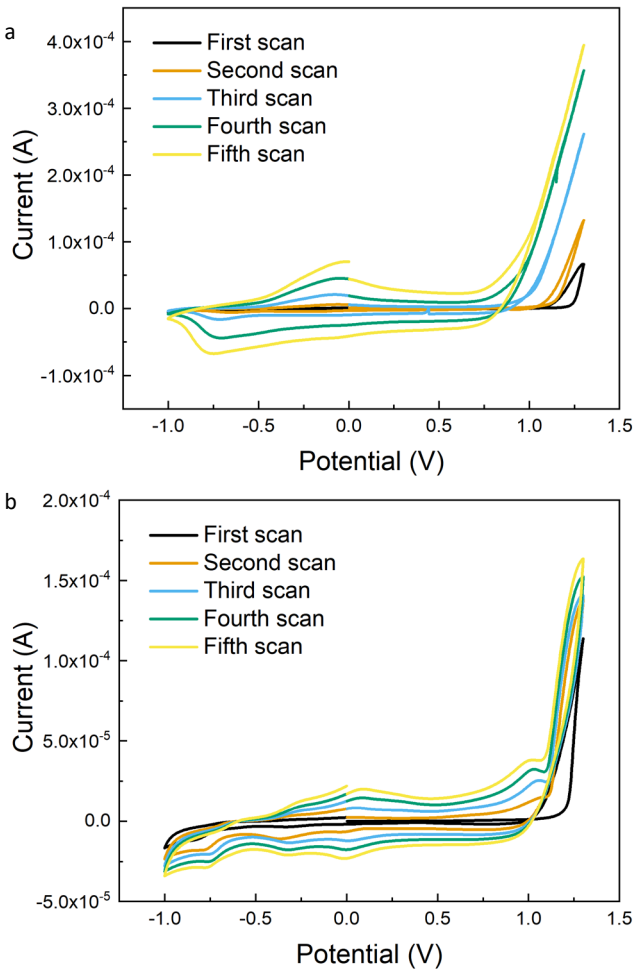

Fig. 3 Potentiodynamic polymerization of (a) EDOT and (b) EDOT-maleimide, including the first five cycles.

time for reaching the conformation or interaction required for polymerization at lower potentials, which was reasonable considering its more complicated molecular structure would require more time to adjust. The determined polymerization potentials of EDOT and EDOT-maleimide were 1.12 and 1.13 V at 5 mVs^{-1} (vs. silver pseudoreference), respectively. The potentials used for potentiostatic deposition were 1.10 V for both EDOT and EDOT-maleimide. This value was chosen to allow for solubility of the oligomers and rate of electrodeposition.

In addition to staircase LSV, staircase CV of EDOT and EDOT-maleimide were also conducted. As shown in Fig. 3, the enclosed area under CV of both EDOT and EDOT-maleimide expanded with more cycles. This data indicates that the materials were electroactive and deposited on the working electrodes in both cases. However, EDOT exhibited a substantially higher current response than EDOT-maleimide, which was presumably due to the faster electrodeposition of EDOT. Two well-defined anodic and cathodic peaks, -0.05 and -0.75 V, in EDOT CV (Fig. 3a) explicitly illustrated the doping/dedoping that occurred during cycling. The same peak-to-peak difference was also reported elsewhere.[33] Additionally, the irreversible peak beyond 1.0 V that existed in all cycles was identified as the polymerization peak which was also identified in EDOT-maleimide (Fig. 3b) and

has been seen in other EDOT derivatives.[33] In contrast to the CV of EDOT, the CV of EDOT-maleimide possessed some extra peaks excluding redox peaks centered around 0 V and polymerization peaks beyond 1.0 V. After studying the CV of monomer free electrolyte, the tail at -1.0 V could be reliably ascribed to the effect of solvent. The pair of one anodic and one cathodic peak located at 1.01 and -0.33 V were tentatively assigned to the oxidation and reduction of dissolved oxygen (Fig. S1).[41] The left cathodic peak at -0.78 V was presumed to be due to the reduction of maleimide functional groups but further studies need to be done for detailed verification.[37] Moreover, reversible electrochromic behavior was observed in both cases during the anodic and cathodic sweeps, directly substantiating the formation of conjugated polymers able to undergo reversible doping and dedoping reactions on the working electrode (Supplementary Video1).

Surface Chemistries of PEDOT and PEDOT-maleimide

To study the surface chemistries of the electrodeposited PEDOT and PEDOT-maleimide. XPS survey scans were collected from 0 to 1200 eV (Fig. 4a). The striking difference between PEDOT and PEDOT-maleimide survey scans was the appearance of a strong nitrogen 1s (N 1s) signal at 400.30 eV originating from the attachment of maleimide groups.[42] The other assigned signals in PEDOT were all replicated in PEDOT-maleimide. For high-resolution XPS spectra, a Shirley-type baseline was subtracted prior to fitting and deconvoluting peaks. Fig. 4b includes the experimental N 1s signals of PEDOT and PEDOT-maleimide and fitted lines based on the raw data. Except for the predominant N 1s peak of PEDOT-maleimide that was already seen in the survey scan, a small signal was seen in the PEDOT at 400.10 eV in high-resolution mode and it was believed to come from the residual acetonitrile used as the solvent for all electrodeposition in this work.[43]

Besides the surface chemistry, it is also possible to extract information about doping levels from XPS. Two methods were

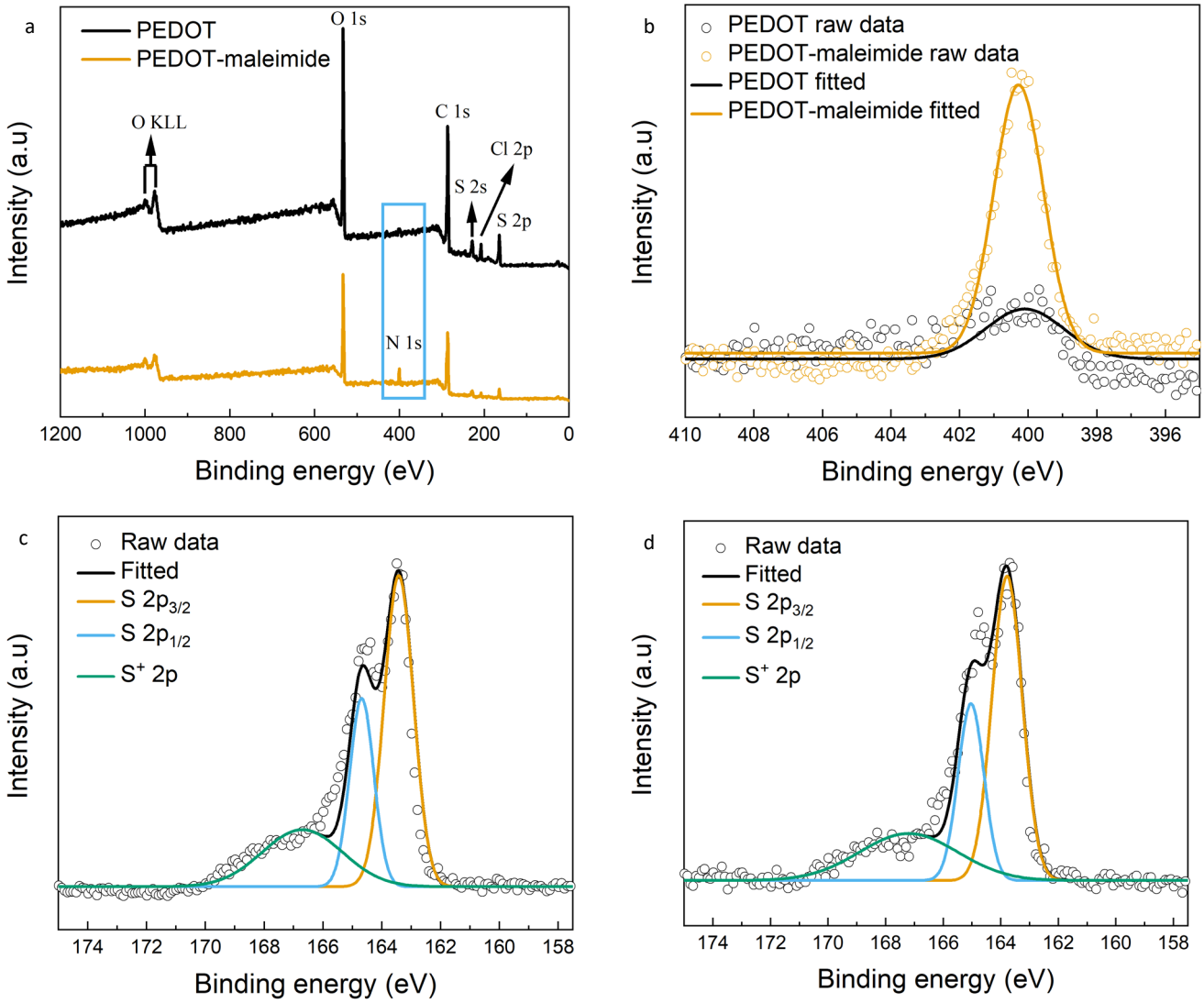

Fig. 4 XPS spectra of PEDOT and PEDOT-maleimide, and their corresponding fitted curves. (a) Survey scan, (b) N 1s, and S 2p of (c) PEDOT and (d) PEDOT-maleimide. The cyan frame in (a) highlights the emergence of the N 1s signal.

Table 1 Deconvoluted sulfur peak positions and doping levels of PEDOT and PEDOT-maleimide

Sample	S $2p_{3/2}$ (eV)	S $2p_{1/2}$ (eV)	S^+ 2p (eV)	Doping level
PEDOT	163.4	164.5	166.7	0.25
PEDOT-maleimide	163.8	165.0	167.2	0.21

used to verify the reliability of the deduced values. During doping, counter ions diffuse into electrode materials for neutralizing the oxidized thiophene. Hence, the areal ratio of oxidized thiophene over the whole sulfur 2p (S 2p) or the atomic ratio of chlorine and sulfur can both be designated as the doping level of the studied electrode material.[44] Before studying the doping level, deconvolution of sulfur signals was necessary to determine the contribution from oxidized sulfur (S^+ 2p). As reported elsewhere, the S^+ 2p peak usually appears after the S $2p_{3/2}$ and $2p_{1/2}$ peaks that are expected to hold a 2:1 areal ratio.[45] Accordingly, the corresponding deconvolutions of S 2p signals of PEDOT and PEDOT-maleimide are shown in Fig. 4c and 4d. The deconvoluted peak positions and deduced doping levels are tabulated in Table 1. The peak splitting of the S 2p was 1.1 and 1.2 eV, respectively, for PEDOT and PEDOT-maleimide which agrees well with what has been determined previously.[45] The positions of all deconvoluted peaks of PEDOT-maleimide were found to be slightly upshifted in comparison to PEDOT, which is likely due to the electron-withdrawing effect from the maleimide functional groups.[46] Based on the calculated doping levels in Table 1, PEDOT was highly doped (0.25 versus 0.21) and this tendency was also consistent with the atomic ratios of chlorine and sulfur in both materials, 0.20 versus 0.16 (Fig. S2 and Table S1).

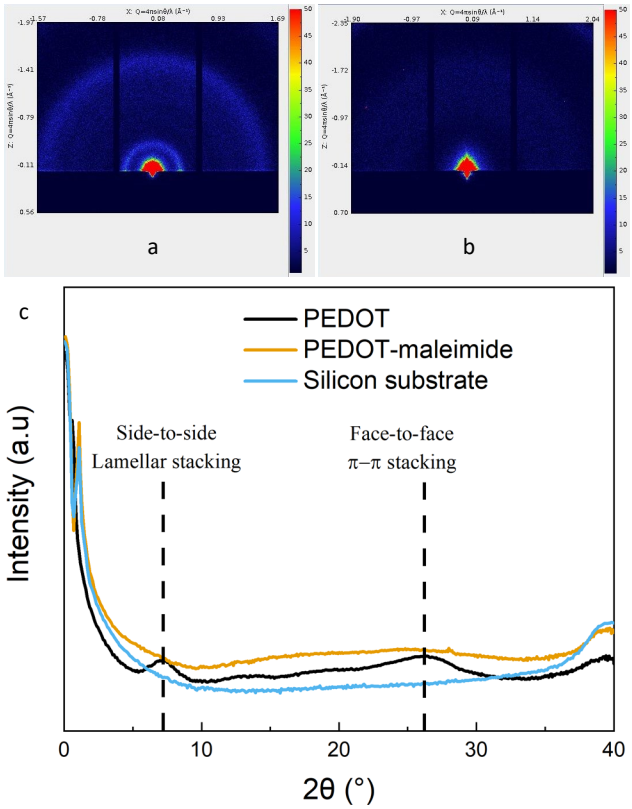

Fig. 5 GIWAXS patterns of (a) PEDOT and (b) PEDOT-maleimide along with their (c) azimuthal integrations.

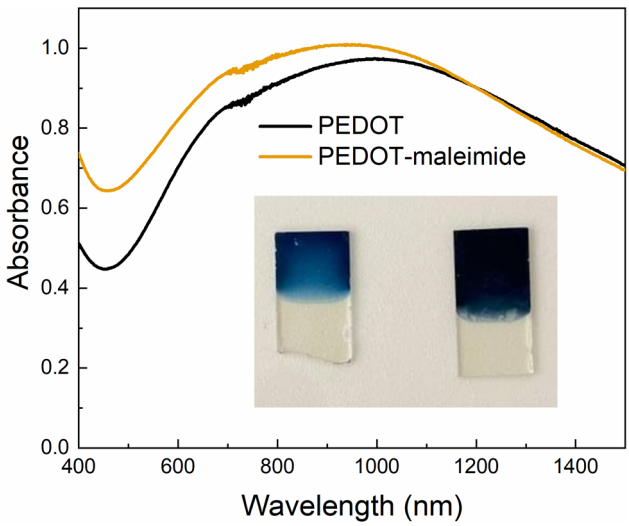

Fig. 6 Normalized UV-vis spectra of PEDOT and PEDOT-maleimide. The inset is the digital picture of (left) PEDOT and (right) PEDOT-maleimide coated ITO samples. The blue part is the deposited film.

Microstructures of PEDOT and PEDOT-maleimide

By virtue of the attachment of maleimide groups on ethylenedioxy rings in PEDOT, the side-to-side (lamellar) stacking order of PEDOT-maleimide was expected to be disrupted to some extent with respect to pristine PEDOT. To quantify the possible structural transformation from PEDOT to PEDOT-maleimide, GIWAXS was conducted. X-ray diffraction patterns of PEDOT and PEDOT-maleimide are shown in Fig. 5a and 5b. The much dimmer scattering halos seen in PEDOT-maleimide in contrast to PEDOT indicate the diminished crystallinity because of the introduced maleimide groups adding extra steric hindrance for stacking. Azimuthal integrations of those patterns were calculated and are plotted in Fig 5c. The disappearance of the side-to-side (lamellar) stacking peak around 7.3° (d~1.21 nm) in PEDOT-maleimide reveals the more disordered nature of these films. The face-to-face (π-π) stacking order was also disrupted, as the peak around 26.2° (d~0.34 nm) in PEDOT was hardly discernable at all in PEDOT-maleimide.[47,48]

UV-vis Spectra of PEDOT and PEDOT-maleimide

PEDOT and PEDOT-maleimide coated ITO samples, the same as those used in XPS, were subjected to UV-vis and the recorded spectra are presented in Fig. 6. In Fig 6, the attachment of maleimide functional groups on PEDOT posed almost no changes in the overall UV-vis absorption pattern, except for some small offsets in intensity. Both PEDOT and PEDOT-maleimide films showed the typical deep blue color of PEDOT as shown in the inset.[17,46] Furthermore, the humps evident at 1000 nm in both materials are signs of the PEDOT being doped, contributed by the absorption from polaron/bipolaron

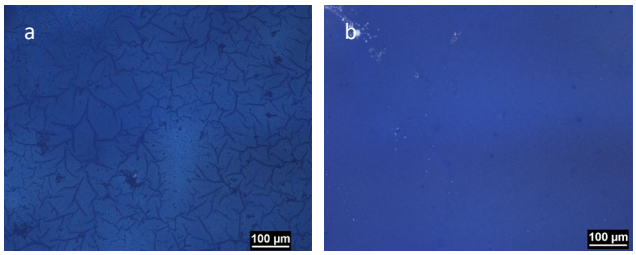

Fig. 7 OM of (a) PEDOT and (b) PEDOT-maleimide ITO samples at high magnification.

excitation. This was also in agreement with the previously discussed results from XPS.

Morphologies of PEDOT and PEDOT-maleimide

The same coated ITO samples were delivered for OM as well as C223BT samples used for the electrochemical studies. Even though the macroscopic visual appearance of PEDOT and PEDOT-maleimide was similar, their textures under the optical microscope were substantially different, especially in those ITO samples. As presented in Fig. 7a and S2a, relatively large creased features, or wrinkles, were pervasive on the surface of PEDOT in both magnifications, while the surface of PEDOT-maleimide was essentially free of such creases or other types of features (Fig. 7b and S2b). The images of C223BT samples also showed better homogeneity of the PEDOT-maleimide samples on gold substrates (Fig. S3c and S3d).

In the wake of these OM results, SEM was applied to further explore the more subtle differences of PEDOT and PEDOT-maleimide at smaller scales. At low magnifications (Fig. 8a), the same creased features were again observed.[17] PEDOT-maleimide was also flat at that magnification (Fig. 8b). Moving to the higher magnifications, some globules formed on the PEDOT surface while PEDOT-maleimide was essentially free of them and instead showed a nanofibrillar structure (Fig. 8c and 8d). The diameters of these pervasive nanofibrils on the PEDOT-maleimide surface were determined to be around several tens of nanometers (Fig. 8d). The size of pores was around several tens to hundreds of nanometers. However, PEDOT itself did not show any nanofibrillar structures (Fig. 8c). Other magnifications are included in Fig. S4. Owing to the porous structure of PEDOT-maleimide, it was expected to possess a higher effective surface area than PEDOT. The nature of the surface roughness of PEDOT-maleimide was also a function of length scale. PEDOT-maleimide was clearly smoother than PEDOT at large length scales (above ~1 µm), but seemingly rougher than PEDOT at small length scales (below ~1 µm) (Fig. 8 and S4). The comprehensive and detailed studies regarding the effective

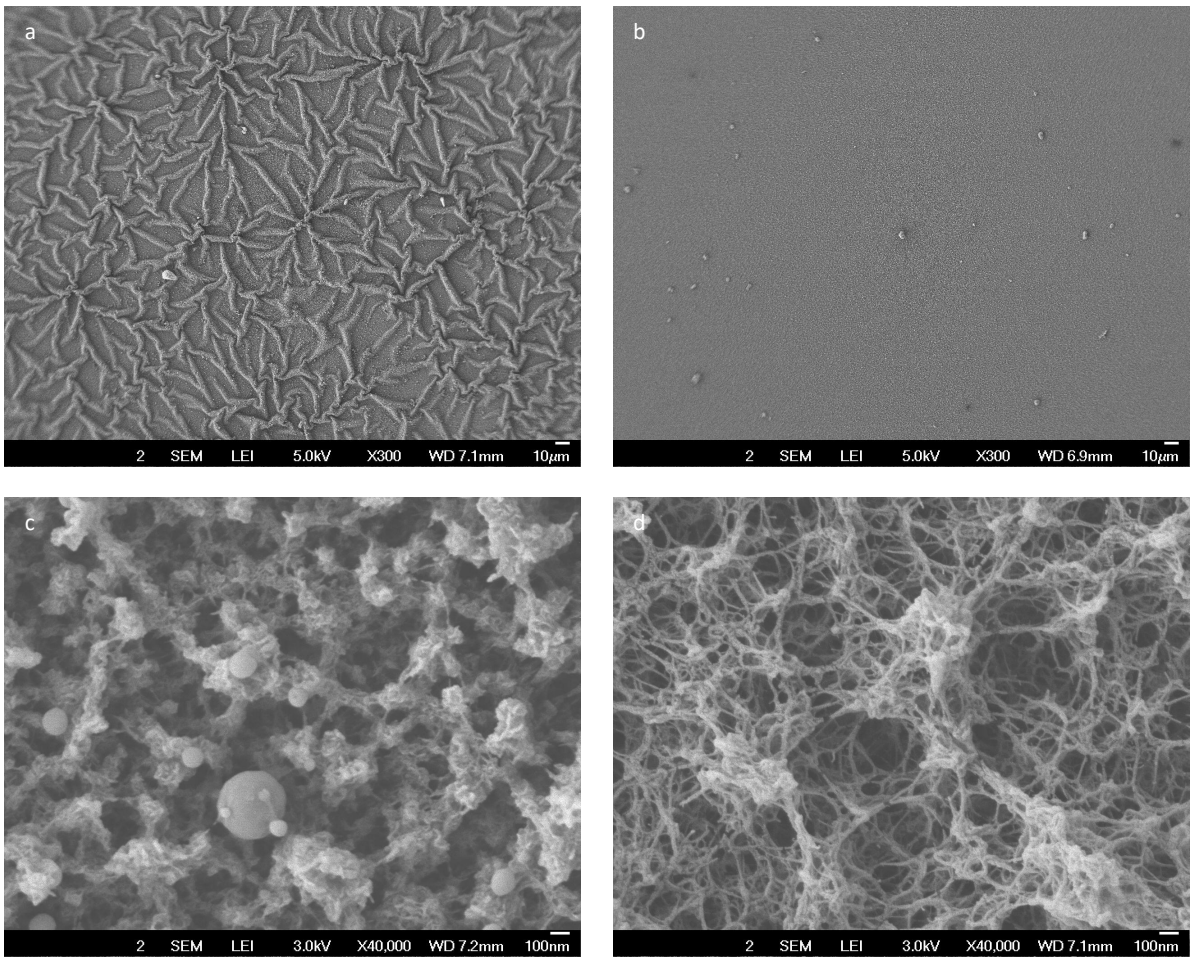

Fig. 8 SEM of PEDOT at (a) low magnification, (c) high magnification and PEDOT-maleimide at (b) low magnification, (d) high magnification.

surface area and surface roughness were investigated using AFM.

The origin of those creases formed on ITO was presumably related to the swelling and drying of electrode materials, as discussed in our previous publications.[17] When more cross-linking agents were used for electrodeposition, fewer creases or wrinkles were formed because of less deformation during swelling and drying cycles. The fact that the PEDOT-maleimide films were less wrinkled suggests that they have higher mechanical properties.

Electrical Conductivities of PEDOT and PEDOT-maleimide

By virtue of the diminished crystallinity observed in PEDOT-maleimide through GIWAXS, it was suspected that the electrical conductivity might be impaired as well. The positive impact of the crystallinity on the electrical conductivity of PEDOT:PSS films has been reported elsewhere.[49, 50] The sheet resistance (R_{sheet}), and thickness (T) of PEDOT and PEDOT-maleimide coated ITO samples were collected. Their conductivities (σ) were derived from the following equations:

$$\mathbf{R_{sheet}} = \frac{\pi}{\ln 2} \cdot \mathbf{R_g} \cdot \mathbf{R_r} \quad (1)$$

$$\boldsymbol{\sigma} = \frac{1}{\mathbf{T} \cdot \mathbf{R_{sheet}}} \quad (2)$$

T denotes the thickness of the tested thin film estimated from the cross-section images (Fig. S5). R_g is a geometric factor dependent on the dimension of the thin film (0.6×1 cm^2) and the tip spacing (1 mm) of the four-point probe. According to the handbook of Haldor Topsoe,[51] the value of Rg is 0.8 for our geometry. R_r represents the resistance directly displayed on the meter during each measurement. The thickness and sheet resistance of all characterized samples were tabulated in Table S2 and S3.

According to Table S2, PEDOT and PEDOT-maleimide possessed a similar film thickness of around 450 nm which is about one third of what we expected from the empirical equation.[39] This was possibly due to the different current collectors, the solvents, and the specific set-up used for accommodating the electrodeposition. Besides, the averaged sheet resistance of PEDOT-maleimide increased by five times in contrast to PEDOT, from 6.65 kΩ to 38.9 kΩ (Table S3). As the consequence, the electrical conductivity of PEDOT is almost six times of that of PEDOT-maleimide, 3.34±0.17 and 0.58±0.04 S cm^{-1}, respectively (Table S4). This drop was presumably due to the substantially lower crystallinity of PEDOT-maleimide as revealed by GIWAXS.

Mechanical properties and Roughness of PEDOT and PEDOT-maleimide

During the preparation of ITO and silicon samples, it was found that PEDOT-maleimide could be easily detached as an intact film from the substrate, but PEDOT films fell apart into multiple small pieces when the same detachment protocol was followed. PEDOT-maleimide films were also able to be readily handled by tweezers, which was extremely difficult if not impossible for PEDOT. It was observed that the PEDOT-maleimide films would substantially fold if they were taken out of the water, but once they were put back to the water interface, they would unfold back to their original size (Supplementary Video2). We also found that PEDOT-maleimide films were more resistant to the deformation induced during four-point probe measurements which require a constant pressure to ensure close contact between the electrode pins and the sample surface. After measurements, PEDOT-maleimide showed no obvious holes while every PEDOT sample tested showed evidence for damage near the pin positions (Fig S6).

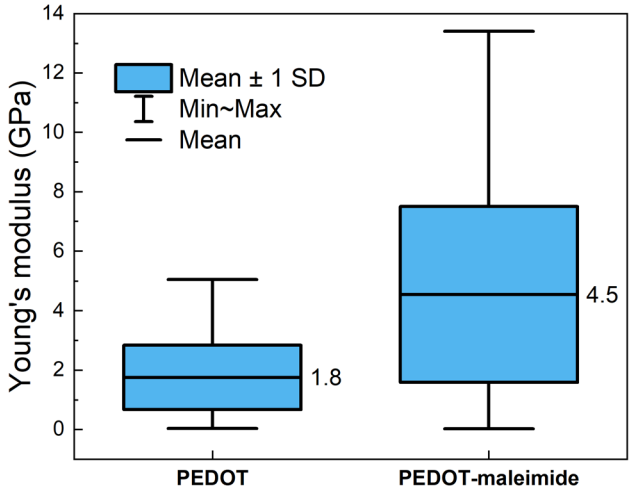

Fig. 9 Young's modulus distribution of PEDOT and PEDOT-maleimide revealed by nanoindentation.

Traditional mechanical tests are difficult to perform on electrodeposited polymer thin films. Therefore, AFM was selected for evaluating the mechanical properties of the films through nanoindentation. Representative topographies of 1×1 μm^2 mapping areas for nanoindentation of PEDOT and PEDOT-maleimide are shown in Fig. S7. The Young's moduli of PEDOT and PEDOT-maleimide coated ITO samples were plotted as boxplots and are presented in Fig. 9. Interquartile range was

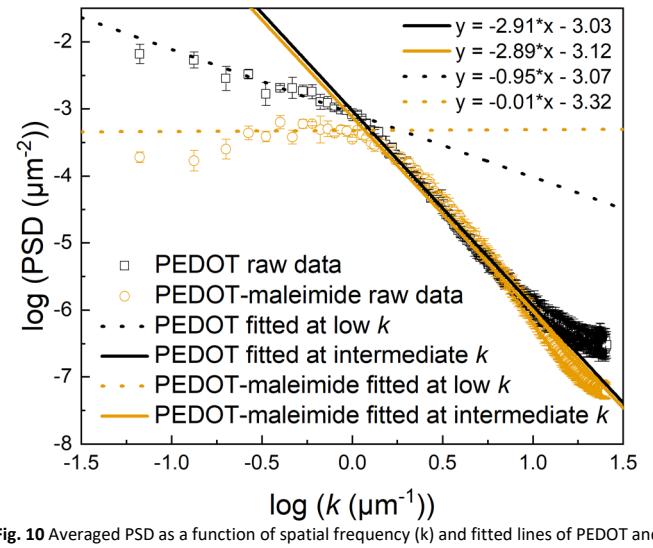

Fig. 10 Averaged PSD as a function of spatial frequency (k) and fitted lines of PEDOT and PEDOT-maleimide.

Table 2 β of fitted lines and calculated FD of PEDOT and PEDOT-maleimide

Sample	β_{solid}		β_{dash}		FD_{solid}		FD_{dash}	
	Mean	Deviation	Mean	Deviation	Mean	deviation	Mean	deviation
PEDOT	2.91	0.02	0.95	0.04	2.05	0.01	3.03	0.02
PEDOT-maleimide	2.89	0.02	None	None	2.06	0.01	None	None

Table 3 RMS roughness of PEDOT and PEDOT-maleimide at different length scales

Sample	1×1 μm^2		5×5 μm^2		10×10 μm^2		15×15 μm^2	
	Mean (nm)	Deviation (nm)	Mean (nm)	Deviation (nm)	Mean (nm)	Deviation (nm)	Mean (nm)	Deviation (nm)
PEDOT	74.2	15.7	136.7	12.1	132.7	5.5	193.7	6.1
PEDOT-maleimide	85.3	7.2	115.3	6.5	112.0	9.5	111.7	3.2

chosen to rule out outliers of the dataset for getting an accurate estimation of the averaged Young's moduli and their deviations. The PEDOT-maleimide displayed a larger overall Young's modulus by comparing the width of the boxplot. The averaged Young's modulus of PEDOT was 1.8±1.1 GPa and that value of PEDOT-maleimide was 4.5±3.0 GPa. Furthermore, to verify whether differences of means and variances of Young's moduli of PEDOT and PEDOT-maleimide were statistically significant, Z- and F-test were done at a level of significance of 0.05. As test results included in Table S5 and S6 demonstrate, both the means and variances of PEDOT and PEDOT-maleimide were statistically significantly different. Thus, PEDOT-maleimide was more mechanically rigid than PEDOT. This ought to lead to improved cyclic stability as the films should be able to better withstand the imposed deformation caused by the associated ion drifting.

The Young's modulus of PEDOT obtained in this work agreed well with those reported by others. Electrodeposited PEDOT doped with perchlorate in Baek et al.'s work, the same as this work, gave a 1.3±0.7 GPa nanoindentation modulus.[52] A Young's modulus of 0.8±0.2 GPa was determined utilizing similar samples and methods like this work.[17] Tensile tests of electrodeposited PEDOT gave estimates of Young's modulus from 2.0 to 2.5 GPa based on preparation conditions.[53] The Young's modulus of poly(3,4-ethylenedioxythiophene):polystyrene sulfonate (PEDOT:PSS) was reported to be around several GPa by others, for instance, Okuzaki et al. (1.1±0.3 GPa for fibers and 1.8±0.2 GPa for films) and Lang et al. (2.8±0.5 GPa at 23% room humidity).[54] With respect to PEDOT, PSS has usually been considered as the softer part of the PEDOT:PSS composite blends. Research on wet-spinning of PEDOT:PSS have achieved close to 17 GPa Young's modulus by removing excessive PSS and inducing crystallization of PEDOT simultaneously.[55]

In order to quantitatively examine the difference in surface roughness observed by SEM, the PSD analysis was performed on PEDOT and PEDOT-maleimide ITO samples over an area of 15×15 μm^2. Representative topographies of them are presented in Fig. S8g and S8h. The PSD is determined by doing the Fourier transform of the height of each data point, and then averaging squares of the transformed value. The spatial frequency (k) range is defined by the length scale and resolution, which in this case is from 0.07 to 25.6 μm^{-1}.[56] According to dynamic scaling theory, there is a relationship between PSD and k over the limited range of length scale:[57]

$$\mathrm{PSD} \propto k\hat{}(-\beta) \quad (3)$$

here β is the power-law exponent and can be resolved by plotting log (k) against log (PSD), and then carrying out linear fitting. Once it is resolved, the corresponding fractal dimension (FD) is computed using the following equation:[56,58]

$$\mathrm{FD} = \frac{(7-\beta)}{2} \quad (4)$$

The curves of log (k) versus log (PSD) of PEDOT and PEDOT-maleimide are shown in Fig. 10. It was found that both materials were constituted by three different regimes, corresponding to low, intermediate, and high frequencies. The flat region at the high-frequency range ends at a length scale of about 50 nm implying that there is no significant variation of the height profile below this length scale. This could possibly be caused by inherent characteristics of the surface or may be due to the probing limitation of the equipped AFM tips, which have an average tip radius around 15 nm. The increasing linear regime at the intermediate-frequency range has a reasonably constant slope indicating the self-similarity of the growth pattern in this region.[58] The linear fitting was carried out in this range of both PEDOT and PEDOT-maleimide. Their corresponding fitted lines were drawn into Fig. 10 as solid lines. The values of β_{solid} of each fitted line were extracted from their slopes and FD_{solid} of PEDOT and PEDOT-maleimide were calculated and summarized subsequently into Table 2. The FD_{solid} of both materials is basically the same in that regime (2.05 versus 2.06) which is not surprising due to their almost overlapped PSD values over the intermediate-frequency regime. However, the fact that PEDOT-maleimide exhibits slightly higher PSD than PEDOT is also clear (mainly from 1.78 to 7.94 μm^{-1} equal to length scale from 0.13 to 0.56 μm), which could be interpreted as PEDOT-maleimide is slightly rougher than PEDOT over that spatial frequency range (or length scale range). This is in agreement with the observation under SEM (Fig. 8c and 8d). The crossover points in Fig. 10, of both materials, from intermediate to low frequency, were determined to be around 1.10 μm^{-1}. The length scale

corresponding to this spatial frequency was 0.91 μm.[59] Beyond this crossover, PEDOT-maleimide levels off suggesting the end of self-affine growth, and the roughness starts to become independent of the spatial frequency. On the contrary, PEDOT experiences a slope change, from -2.91 to -0.95, which results in higher FD_{dash}, from 2.05 to 3.03(Table 2). This change in FD values was associated with the wrinkles seen in SEM (Fig. 8a, S4a, and S4c) and AFM at the scale of 15 μm (Fig. S8g). The width of those wrinkles is at the several-μm level which is also the range that the slope becomes -0.95. The presence of two fractal regimes in the PSD spectra was also reported previously in roughness studies of electrodeposited PPy.[56,58] Because PEDOT still increases slowly after the crossover point, the PSD difference between PEDOT and PEDOT-maleimide also extends as the length scale increases. Hence PEDOT-maleimide is smoother than PEDOT at length scales larger than 0.91 μm, which is also consistent with our observations under SEM (Fig. 8a, 8b, and S4).

In addition to PSD analysis, the RMS roughness of PEDOT calculated. As stated before, the rougher surface of PEDOT-maleimide was evident when the images at small length scales were examined. The RMS roughness at each length scale was extracted from their images (Fig. S8) and tabulated into Table 3. As seen in Table 3, the RMS roughness of PEDOT is smaller than PEDOT-maleimide at the length scale of 1 μm. When larger length scales were probed, like 5 μm, the RMS roughness of PEDOT overtook PEDOT-maleimide and this trend was preserved at the larger length scale of 10 μm as well as 15 μm. The relative roughness changes along with the increase of probed length scale revealed by RMS roughness are in agreement with the SEM observations and the PSD analysis. In addition, the RMS roughness of PEDOT increases steadily from small length scale (1 μm) to large length scale (15 μm), while PEDOT-maleimide only increased when the length scale was below 1 μm and remained reasonably constant from 5 μm to 15 μm. This dependence on the probed length scale is also consistent with the PSD analysis presented above. Therefore, both RMS roughness and PSD analysis quantified the same change in relative roughness of PEDOT and PEDOT-maleimide observed before under SEM, which is that PEDOT is rougher at large length scales (above ~1 μm) and PEDOT-maleimide is rougher at small length scales (below ~1 μm).

Except for the roughness discussion, those topographies captured at different length scales were also subjected to the evaluation of their effective surface areas. The effective surface areas were evaluated based on summing the surface areas of all triangles forming among three adjacent points. The corresponding results are tabulated into Table S7. Based on those values in Table S7, it is clear that PEDOT-maleimide possesses a larger effective surface area than PEDOT over all probed length scales, which is in good alignment with the porous morphology observed before under SEM as well as the assumption made based on our observations. This advantage could potentially help PEDOT-maleimide accommodate more charges, in other words, better charge storage capability corresponding to high capacitance.

Electrochemical Properties of PEDOT and PEDOT-maleimide

The electrochemical investigation of PEDOT-maleimide by linear CV was compared with PEDOT and bare C223BT samples. The range of this study was from 0 to 0.5 V (vs. silver pseudoreference) in 0.1 M KCl aqueous solution at a scan rate of 100 mVs^{-1}. The almost rectangular shape of the CV curve for both PEDOT and PEDOT-maleimide and fast current response along the switch of sweep directions confirmed the nearly ideal capacitive behavior of both materials (Fig. 11a).[60,61] Compared to the bare gold electrode, both polymers dramatically increased the charge storage capacity. Since the area encompassed by the CV scan is proportional to the capacitance, the larger area enclosed by PEDOT-maleimide indicates that it has higher capacitance. Though both of them manifested quasi-rectangular CV shapes, the CV curve of PEDOT-maleimide showed more pseudocapacitance contribution from surface redox reactions reflected from the slightly bumped current response in the course of anodic and cathodic sweep, centered around 0.25 V.[61] According to our potentiodynamic studies on EDOT-maleimide, those additional surface redox reactions may derive from the maleimide functional groups.

CV analysis was performed at other scan rates as demonstrated in Fig. 11b and 11c, the black arrow specifies the ascending scan rate. The current response in both materials increased steadily with faster scan rates and the quasi-rectangle shape was preserved in both cases up to 200 mVs^{-1} suggesting their excellent rate performance. For calculating capacitance from CV, the following equation was used: [62]

$$C_A = \frac{\int_{E_s}^{E_f} I(E)dE}{2A(E_f - E_s)v} \quad (5)$$

C_A stands for areal specific capacitance. $\int_{E_s}^{E_f} I(E)dE$ is the enclosed area by a CV scan. A and v are used to represent the area of the working electrode and the scan rate, respectively. The areal specific capacitances of PEDOT and PEDOT-maleimide as a function of scan rate were plotted in Fig. 11d. It was found that PEDOT-maleimide exhibited higher capacitance than PEDOT over the tested scan rate range. The highest value was 5.8×10^{-3} Fcm^{-2} obtained at 25 mVs^{-1}, while it was 5.4×10^{-3} Fcm^{-2} at the same scan rate for PEDOT. The specific capacitance decreasing with the increase of scan rate found in this work is consistent with results seen in other supercapacitors. The retention of capacitance, which was the ratio of specific capacitance at 200 mVs^{-1} over the specific capacitance at 25 mVs^{-1}, of PEDOT was 93.2 % in comparison to 92.6 % of PEDOT-maleimide, as shown in Table 4. The difference of those numbers proposed the slightly better rate performance of PEDOT. The rationale behind this lies in the percentage of the outer surface, more accessible than the inner surface for diffused ions, over the total surface of PEDOT was higher than PEDOT-maleimide, which was correct considering the porous and nanofibrillar structures disclosed by morphological analysis. Also, because of the more accessible outer surface and comparably less accessible inner surface, the specific capacitances of supercapacitors tend to decrease along with the increase of charging rates as the diffusion of ions is the essential

part of charging and discharging.[63] That explained the trend also found in this work, Fig. 11d.

The capacitance contributed by the outer surface, exposed to the electrolyte directly, was denoted as C_{out}. Unlike outer surface, inner surface refers to the surface in cracks, voids, pores, and grain boundaries that is not directly exposed to the electrolyte. Charges can also be stored on the inner surface, but this demands a longer charging time to let ions reach the inner surface. The total capacitance consisting of capacitance from the full-exploited inner and outer surface was termed as C_{total}.[63-65] With an increase of scan rate, less capacitive contribution from the inner surface was realized as ions were unable to reach

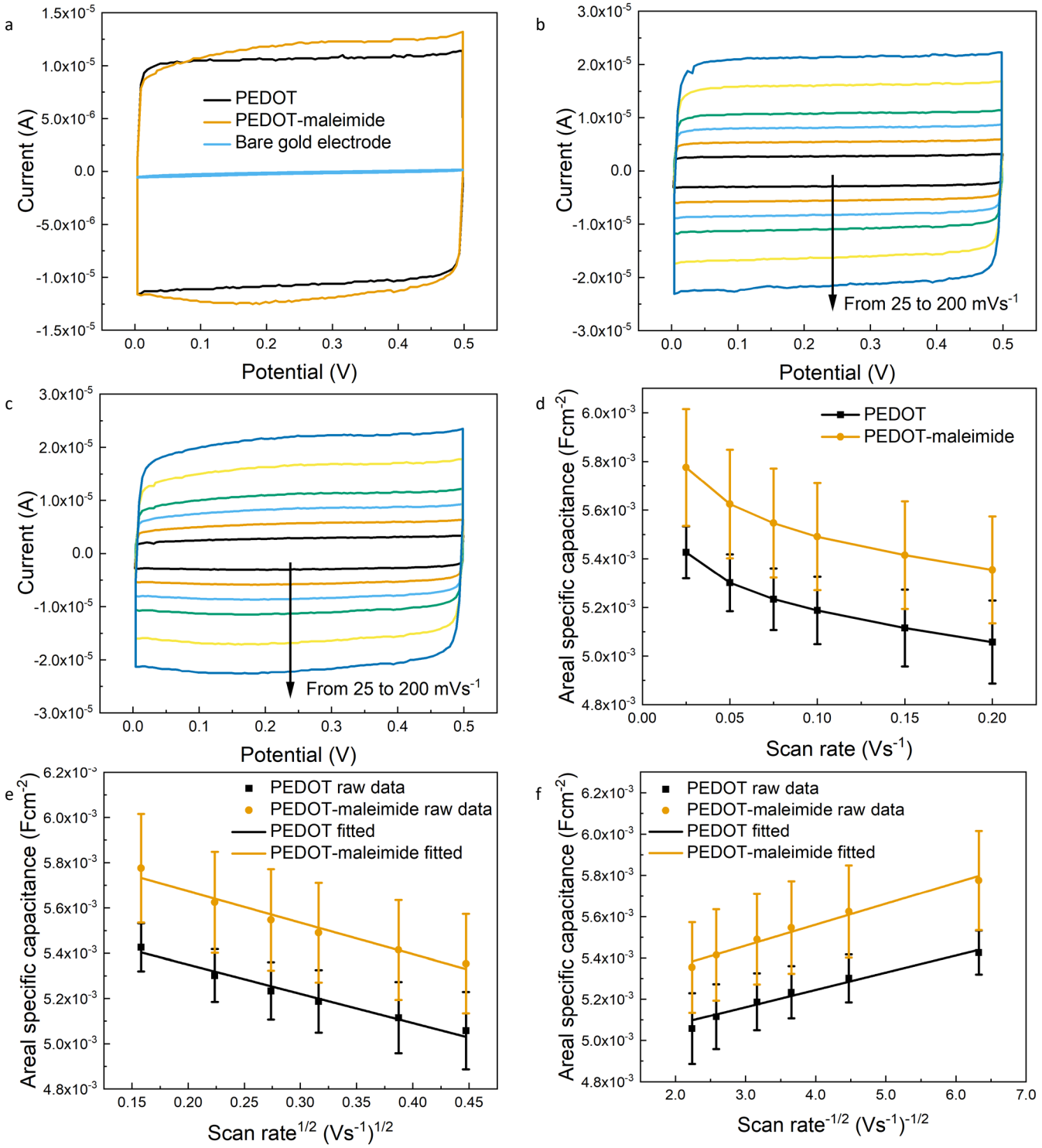

Fig. 11 (a) Linear CV of bare C223BT, PEDOT and PEDOT-maleimide at 100 mVs-1. Linear CV under different scan rates of (b) PEDOT and (c) PEDOT-maleimide. Black arrow specifies the increase of scan rates. (d) Areal specific capacitance of PEDOT and PEDOT-maleimide as a function of scan rate. Areal specific capacitance of PEDOT and PEDOT-maleimide versus (e) Scan rate1/2 and (f) Scan rate-1/2. (All data were averaged over three individual samples)

Table 4 Deduced C_{total} and C_{out}, and their ratios, also including rate performance from CV and GCD

Sample	C_{total} (Fcm^{-2})	C_{out} (Fcm^{-2})	C_{out}/C_{total} (%)	CV-retention (%)	GCD-retention (%)
PEDOT	5.6×10^{-3}	4.9×10^{-3}	87.5	93.2	97.0
PEDOT-maleimide	6.0×10^{-3}	5.2×10^{-3}	86.7	92.6	94.9

the surface before the switch of sweep directions. Therefore, the C_{total} was derived from areal specific capacitance versus the square root of scan rate (C_A *vs.* $v^{1/2}$) by extrapolating the fitting curve to 0, where theoretically the entire inner surface was utilized (Fig. 11e). On the contrary, extrapolation of the fitting curve of areal specific capacitance versus the reciprocal of the square root of scan rate (C_A vs. $v^{-1/2}$) to 0, assuming the scan rate was infinite, which gave out C_{out} instead (Fig. 11f). The calculated C_{out} and C_{total} including their ratios were compiled into Table 4. Not surprisingly, PEDOT received a slightly higher contribution from the outer surface than PEDOT-maleimide, 87.5 % versus 86.7 %, which was consistent with the outcomes of the capacitance retentions and morphologies.

Comparative studies of PEDOT and PEDOT-maleimide were also carried out by GCD. As with linear CV scans, current densities varying from 1.6×10^{-4} to 1.1×10^{-3} Acm^{-2} were selected for detailed study. In order to compare the capacitance derived from GCD with CV, the potential window was kept the same. Again, the isosceles triangle GCD curves depicted in Fig. 12a and 12b of PEDOT and PEDOT-maleimide indicate their closely ideal capacitive behaviors, which was also reflected from quasi-rectangular CV curves. The black arrow points to the increase in the current density. The areal specific capacitances from GCD curves were determined according to the following equation:[66]

$$C_A = \frac{I\Delta t}{\Delta V} \quad (6)$$

where the charging/discharging current density is denoted as I. Δt is the discharging time. ΔV accounts for the charging/discharging potential window. The calculated areal specific capacitances were plotted into Fig. 12c, in which the same inverse relationship was noticed, *i.e.*, the decreased specific capacitance along with the increased current density. Areal specific capacitances derived from GCD curves were comparable to CV, around several $mFcm^{-2}$. The areal specific capacitance of PEDOT-maleimide was also larger than PEDOT at all current densities probed in this work. The maximum value was 7.0×10^{-3} Fcm^{-2} at 1.6×10^{-4} Acm^{-2} as opposed to 6.3×10^{-3} Fcm^{-2} of PEDOT. Additionally, areal specific capacitances of PEDOT provided in this work are similar to what other investigators have reported, around several to tens $mFcm^{-2}$.[27,67] The capacitance retention at the largest current density was also calculated and organized into Table 4. This time, the retained percentages of both materials were somewhat higher than CV but PEDOT still surpassed PEDOT-maleimide.

Equivalent serial resistance (ESR) or internal resistance, R_{ESR}, includes the ohmic resistance of the electrolyte and electrode materials, and contact resistance across the interfaces,[68] which is typically evaluated by the IR drop appearing during the charging/discharging transition point of GCD or the intercept on the x-axis of the Nyquist plot.[69] R_{ESR} is a crucial parameter for evaluating the performance of supercapacitors. The following equation was used to calculate R_{ESR} via the IR drop:[69]

$$R_{ESR} = \frac{\Delta U}{2AI} \quad (7)$$

IR drop at the charging/discharging transition point is represented by ΔU. On the basis of Equation (7), the IR drop is enlarged if a larger charging/discharging current flows. Fig. 12d accurately copied the trend as just specified. The half of the slope of the fitted line passing origin was designated as the R_{ESR}/A of the corresponding material. The R_{ESR} of PEDOT was found at 164.2±4.1 Ω and that value of PEDOT-maleimide was 168.3±3.0 Ω. Considering Equation (11), close power densities are supposed to be obtained because of the close R_{ESR} discovered above.

Coulomb efficiencies, describing the charge transfer reversibility of charge storage devices,[70] of PEDOT and PEDOT-maleimide were also investigated. As one of the attributes of supercapacitors, the coulomb efficiency supposedly should approach 100 %. Coulomb efficiencies declined by 4 ~ 5% in both PEDOT and PEDOT-maleimide at higher current densities (Fig. 12e). Equation (8) was used to compute the coulomb efficiency. Only charging and discharging time is required in this equation because of the nearly ideal capacitive behaviors of PEDOT and PEDOT-maleimide.

$$\eta\ (\%) = \frac{t_{discharging}}{t_{charging}} \times 100 \quad (8)$$

For the convenience of comparing the performance of PEDOT and PEDOT-maleimide, a Ragone plot was utilized, which consisted of energy density (E) and power density (P). Equation (9) and (10) were used to calculate those values for PEDOT and PEDOT-maleimide and they were subsequently plotted into Fig. 12f. Those equations were presented as follows:[5,66]

$$E = \frac{1}{2} \cdot C_A \Delta V^2 \quad (9)$$

$$P_{average} = \frac{E}{\Delta t} \quad (10)$$

$$P_{max} = \frac{\Delta V^2}{4AR_{ESR}} \quad (11)$$

It was observed that PEDOT-maleimide had fast charging/discharging from PEDOT, almost the same power densities, superior charge storage capacity, and larger energy densities than PEDOT. The largest energy density that PEDOT-maleimide achieved was 0.24 $\mu Whcm^{-2}$ at a power density of 39.25 μWcm^{-2}. This find proved the advancement of PEDOT-maleimide, regarding better performance on charge storage.

To further explore the characteristics of PEDOT and PEDOT-maleimide, EIS was performed at 0 V bias with 10 mV amplitude from 10^{-1} to 10^{5} Hz. The relevant results are shown in Fig. 13. The PEDOT-maleimide was not expected to have a comparable impedance behavior as pristine PEDOT. However, the impedance data indicated that both PEDOT-maleimide and PEDOT had essentially similar impedance behavior (Fig. 13a). Nyquist plots of them were likewise analyzed to help determine equivalent circuit models. The fitted curves, from the chosen equivalent circuit model, were presented associated with their raw data in Fig. 13b. In Fig. 13b, one of insets is the model used

in this work, including a simplified Randles circuit model and a generalized finite-Warburg in series, the other is the high-frequency range of Nyquist plots which shows the distorted semi-circle in both of them. The simplified Randles circuit employed for modeling in this work has been commonly adopted to describe the faradic reactions taking place on the polarized electrode surface, similar to this work.[71-73] In this circuit, R_S is the modeled internal resistance or equivalent serial resistance, which by theory is equivalent to the above-extracted R_{ESR}. This number nearly reproduced what was calculated from the IR drop, which was 145.1±6.4 and .145.3±20.0 Ω for PEDOT and PEDOT-maleimide, respectively. Slightly higher resistance

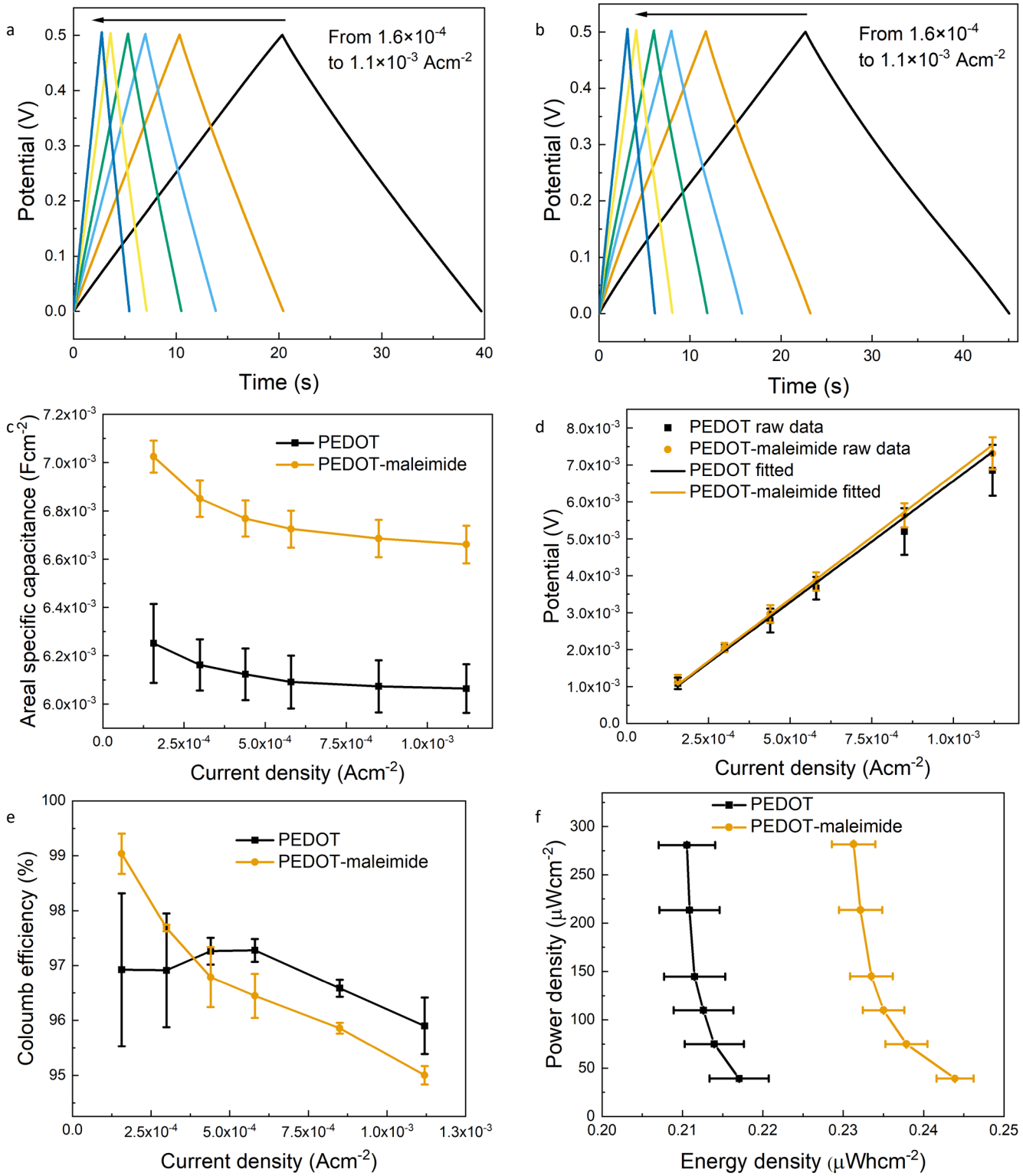

Fig. 12 GCD curves of (a) PEDOT and (b) PEDOT-maleimide at various current densities. (C) Areal specific capacitance of PEDOT and PEDOT-maleimide as a function of current density. (d) IR drop, (e) coulomb efficiency, and (f) Ragone plot of PEDOT and PEDOT-maleimide. (All data were averaged over three individual samples)

was also realized for PEDOT-maleimide but not that much obvious. R_{ct} is the charge transfer resistance used to model the faradic resistance during redox reactions. By comparison, PEDOT-maleimide exhibited higher R_{ct} than PEDOT (14.4±9.6 *vs.* 6.2±2.8 Ω). Not only from the fitted value, visually, the larger radius of the semi-circle in the high-frequency range of PEDOT-maleimide also demonstrates the larger R_{ct} of it (Figure 13b inset). The potential cause for this nearly doubled R_{ct} is presumably due in part to the larger pore size of PEDOT-maleimide that was revealed under the SEM. The studies regarding the deleterious effect of pore size on charge transfer have been published by the group of Inchan,[74] in which they

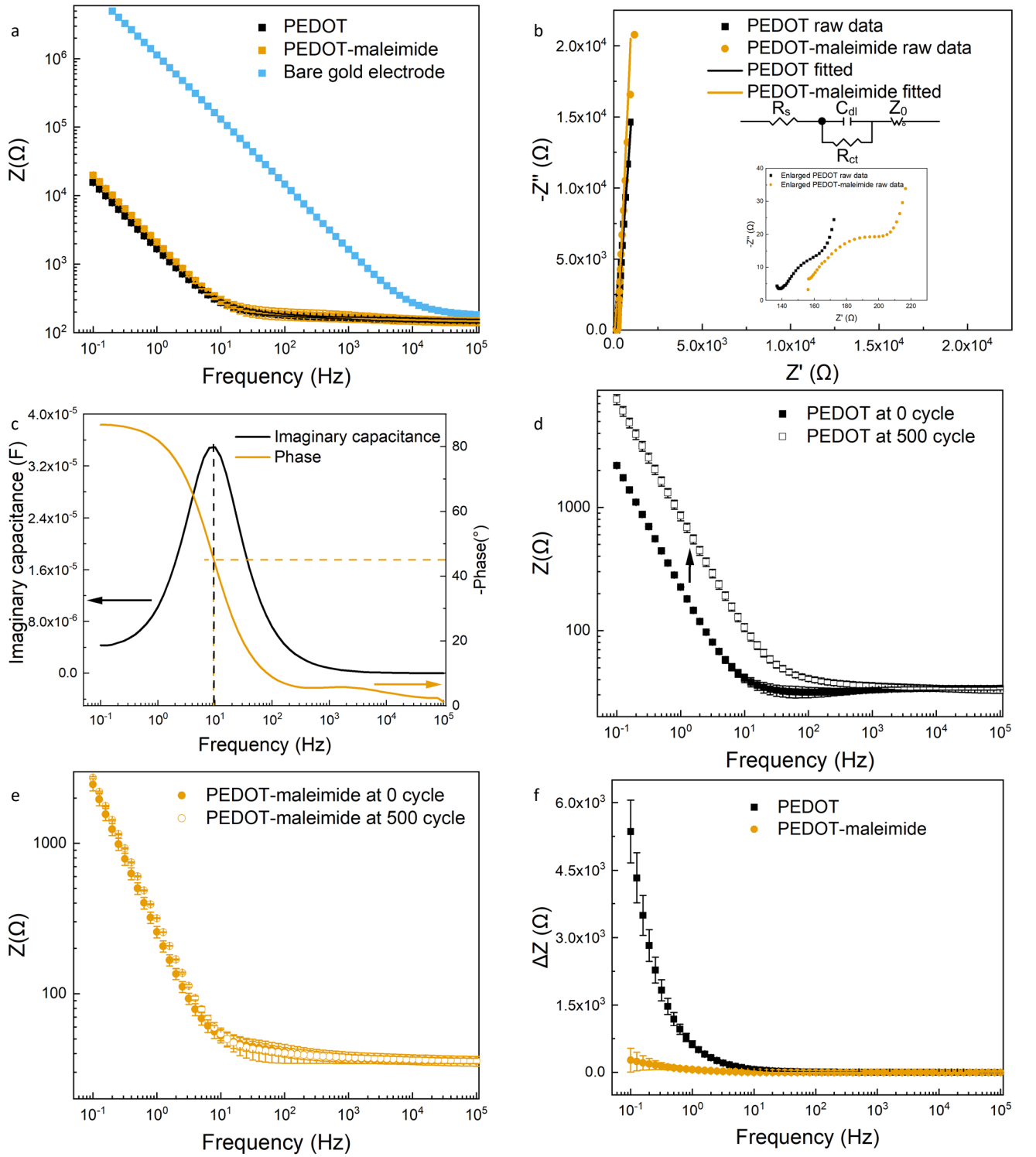

Fig. 13 (a) Impedance behaviors of bare C223BT, PEDOT and PEDOT-maleimide. (b) Nyquist plots of PEDOT and PEDOT-maleimide, and the inset is the applied simplified Randle's circuit model. (c) Evolution of imaginary capacitance and phase angle of PEDOT-maleimide. The impedance changes of C220BT samples after 500 CV cycles of (d) PEDOT and (e) PEDOT-maleimide, and (f) their differences. (All data were averaged over three individual samples)

found that the larger pose size caused the larger R_{ct}. The other potential explanation for the increased R_{ct} is from the less/or non-conductive maleimide functionalities in contrast to the PEDOT backbone. Considering that a portion of the PEDOT-maleimide interface was replaced by the less conductive maleimide functionality from the conductive PEDOT backbone, which is responsible for the electron transport, the charge transfer is undoubtedly hampered. Therefore, larger charge transfer resistance was achieved. C_{dl} corresponds to the double-layer capacitance. The generalized finite-space Warburg element was designated to delineate the ion diffusion existing in the low-frequency regime in Nyquist plots since the slope is larger than one.[75] Overall, the goodness of fit, which is evaluated by χ^2 in this study, remains < ~0.003. Moreover, the nearly vertical Nyquist plot in Fig. 13b again reveals their highly capacitive behaviors.

The relaxation time constant (τ_0) delimiting the boundary of energy-dissipation and energy-storage regions[76] was derived for both materials. Smaller time constants typically correspond to high power delivery and more ideal supercapacitive behavior.[66] There are generally two strategies to calculate the relaxation time constant. The first and relatively easy approach is to find the frequency corresponding to 45° in phase angle versus frequency plot, as shown in Fig. 13c and S9. The reciprocal of that frequency is then taken as the relaxation time constant. The second approach was also presented in Fig. 13c and S9, which was through the imaginary capacitance (C″). According to Equation (12),[64] the plot of imaginary capacitance as a function of frequency was constructed for both PEDOT-maleimide and PEDOT, Fig. 13c and S9. The reciprocal of the frequency where the maximum imaginary capacitance obtained was used as the relaxation time constant in this situation. Auxiliary dash lines were drawn to locate the frequency.

$$C'' = \frac{Z'}{2\pi f |Z|^2} \quad (12)$$

imaginary capacitance is symbolized as C″. |Z| and Z' are impedance magnitude and real impedance. Frequency is designated as *f*. The relaxation time constants found out by those two methods were similar, 108.1±0 and 122.5±6.7 ms of PEDOT and 90.4±15.7 and 92.2±12.6 ms of PEDOT-maleimide, Table S. The slightly lower value that PEDOT-maleimide exhibited corresponds to more efficient ion transport and thus better capacitive expression than PEDOT. The relaxation time constants of both materials (~100 ms) are much lower than similar values for carbon-based electrode materials (~10 s) and are comparable to other pseudocapacitive electrode materials.[64, 66, 76] The larger pore size of PEDOT-maleimide is presumably the cause of lower relaxation time. The phase angles of PEDOT and PEDOT-maleimide at low frequencies were around 87°, indicating that they were both excellent candidates for supercapacitive applications.

Aside from charge storing/releasing capabilities, the cyclic stabilities of PEDOT and PEDOT-maleimide were also examined on C220BT electrodes, as they could be immersed into solutions without any modification. Staircase CV and EIS were coupled for these tests. In the lieu of 0.1 M KCl solution, 1×PBS solution was selected, and staircase CV was performed from -0.8 to 0.8 V at 100 mVs^{-1} for 500 cycles. EIS was carried out before and after 500 cycles in the 1×PBS solution. The characterized changes of impedance behaviors of PEDOT and PEDOT-maleimide are summarized in Fig. 13d-f. The deterioration of electrochemical properties of PEDOT was observed after 500 cycles, as shown in Fig. 13d, while PEDOT-maleimide only upshifted negligibly within the error bar as shown in Fig. 13e. The failure modes of PEDOT were composed of interfacial delamination and structural degradation.[776] The ease in separating PEDOT-maleimide from ITO indicated that the interfacial adhesion between the electrode material and substrate was not significantly enhanced compared with PEDOT. The structural degradation was believed triggered by the expansion and contraction due to ions diffusing in and out in the course of doping/dedoping. Therefore, less deformation of PEDOT-maleimide imposed by the perturbance from ion diffusion was perceived as the cause for the better cyclic stability, due to better mechanical properties as revealed by the nanoindentation characterization (Fig. 9). Fig. 13f included the impedance differences over the whole frequency range of PEDOT and PEDOT-maleimide. The surge in the low-frequency range was indicative of the alteration on the electrodeposited PEDOT, while PEDOT-maleimide only varied slightly. That change was also interpreted as the loss of charge storage capacity, which is unfavorable for supercapacitors.[78] Therefore, PEDOT-maleimide seemingly addressed the stability issue existing in PEDOT.

The self-discharging and leakage currents are two critical parameters delineating the downsides of supercapacitors. Ideally, supercapacitors are supposed to keep their voltages from decreasing when the external circuit is unloaded. Practically, supercapacitors or even capacitors tend to self-discharge because of high internal resistance and this behavior is required to be characterized whenever a new supercapacitor is evaluated.[79] Self-discharging rate is usually high at the beginning and tends to be steady, approaching the end of the recording. On account of this feature and avoiding constantly monitoring the open-circuit potential for a long period, a discharging rate cut off, 10^{-6} Vs^{-1}, was set for stopping the potential monitoring. Fig. 14a presented the self-discharging curves of samples. The PEDOT and PEDOT-maleimide samples both discharged at similar rates in the initial 200 s but the PEDOT-maleimide samples slowed down at early time points and stopped at higher voltages. The average voltage before stopping monitoring of PEDOT-maleimide was 0.38 V, while PEDOT stopped at 0.34 V.

Small leakage currents are required to maintain charges in supercapacitors. The assessment of this parameter is straightforward. Here, it was carried out by recording the current change over an hour-long chronoamperometry at 0.5 V (Fig. 14b). Since the whole cell was completely discharged before testing, the first 20 s in Fig. 14b was the charging time before reaching 0.5 V. The time after 20 s was when the current undulation took place, that was the synergetic effect of charging and self-discharging. Hence, the leakage current of PEDOT and PEDOT-maleimide both fell into the range between 0.01 and 0.1 μA and their difference was indiscernible.

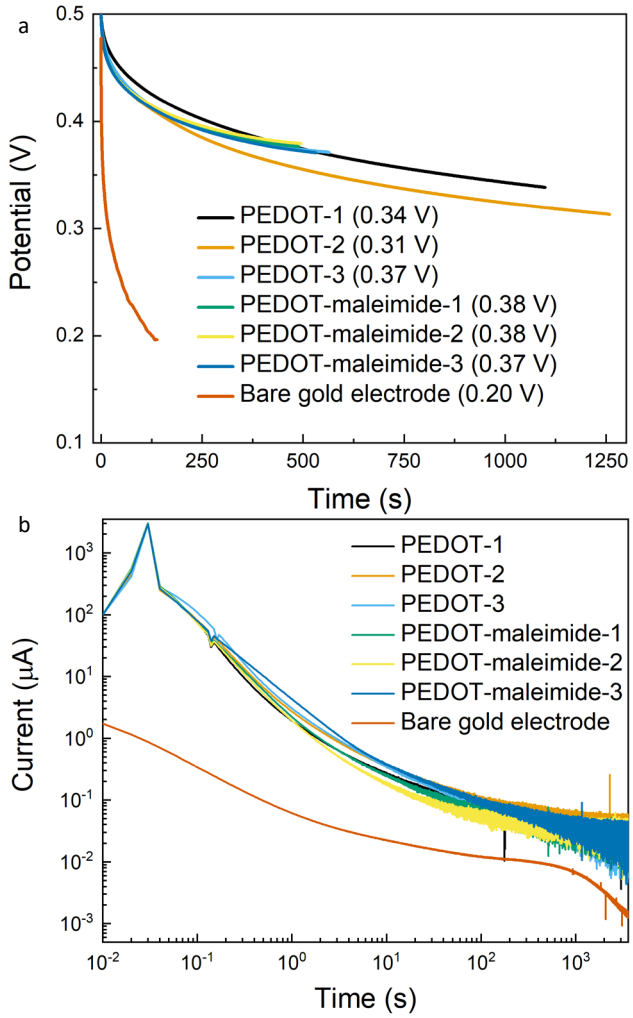

Fig. 14 (a) Self-discharging with a cutoff at 10-6 V s-1 and (b) leakage currents for an hour of three PEDOT and PEDOT-maleimide C223BT samples as well as a bare electrode.

A bare electrode was also characterized regarding those two parameters and is included in Fig. 14a and 14b. The striking discrepancies of its voltage and current response as a function of time as opposed to those two CPs again are evident for the successful electrodeposition of materials with large charge storage capacities.

Conclusions

PEDOT-maleimide was thoroughly investigated concerning its possibility to replace PEDOT for supercapacitive applications. The electrodeposition was adopted to prepare samples for characterization by a wide variety of complementary techniques. Surface chemistries were studied by XPS and the successful electrodeposition of PEDOT-maleimide was confirmed by the appearance of N 1s peak. Based on GIWAXS results, the maleimide substitution disrupted the stacking order in both the side-to-side (lamellar) and face-to-face (π-π) stacking directions. This impact on the microstructure resulted in five times lower electrical conductivity compared to the pristine PEDOT, from 3.34±0.17 down to 0.58±0.04 S cm^{-1}. The UV-vis absorption curve of PEDOT-maleimide resembled that of PEDOT which indicated that both of them were doped in agreement with XPS data. Both OM and SEM studies showed a dramatic morphological transformation from bumpy and heterogeneous (for PEDOT) to porous and homogeneous (for PEDOT-maleimide). The effective Young's modulus increased, from 1.8±1.1 to 4.5±3.0 GPa, after the attachment of maleimide functional groups. AFM was also used to study the roughness differences, and it turned out PEDOT-maleimide was slightly rougher than PEDOT at small length scales (~1 μm and below) but smoother at large length scales (~1 μm and above). This change in relative roughness was also seen in SEM images taken at different magnifications.

In terms of supercapacitive performance, PEDOT-maleimide exhibited higher areal specific capacitance in 0.1 M KCl as opposed to PEDOT, which was cross-validated by linear CV and GCD, 5.8×10^{-3} (25 mVs^{-1}) or 7.0×10^{-3} (1.6×10^{-4} Acm^{-2}) Fcm^{-2}. As the consequence, higher energy densities were also obtained by PEDOT-maleimide, while the power densities were comparable to PEDOT. The possible cause for this increase in capacitance correlates with nanofibrillar and porous morphology of PEDOT-maleimide that can facilitate ion transport,[30] the larger effective surface area that can accommodate more charges,[80] as well as attached redox active maleimide functional groups that can contribute extra capacitance.[18] Shorter relaxation time constants also indicate faster ion transport in PEDOT-maleimide. The linear CV scans reflected the occurrence of surface redox reactions, which may come from attached maleimide functional groups. This is supported by the observation of an emergent reduction peak in the potentiodynamic polymerization of EDOT-maleimide by staircase CV. In addition to their charge storing/releasing capabilities, the cyclic stability of PEDOT-maleimide was also much better than PEDOT. The performance of PEDOT-maleimide remained stable, while PEDOT impedance increased significantly after 500 CV cycles. This improvement of PEDOT-maleimide was related to its higher mechanical stiffness presumably due to limited cross-linking among maleimide functional groups.[81] In addition, the charge transport of PEDOT-maleimide determined by EIS was essentially the same as that of pristine PEDOT, even though the molecular stacking determined by GIWAXS was substantially compromised.

Overall, the studies in this work have established the better supercapacitive performance, mainly through the higher specific capacitance, and better cyclic stability, of PEDOT-maleimide over PEDOT. The improvements of PEDOT-maleimide may also offer opportunities to replace PEDOT in other applications like organic electrochemical transistor (OECT) where their higher capacitance and stability may lead to longer operational lifetime and higher sensitivities.[82] In the future, the presence of the reactive maleimide moiety is expected to provide many opportunities for further functionalization to optimize these PEDOT-based films for specific performance requirements.

Author contributions

The manuscript was written through the contributions of all authors. All authors have given approval to the final version of the manuscript. SSN: Investigation, Methodology, Writing-Review&Editing. YW: Conceptualization, Methodology, Investigation, Validation, Formal analysis, writing-Original draft, Writing-Review&Editing, Visualization. PS: Writing-Review&Editing. SC: Writing-Reviewing&Editing. JL: Writing-Reviewing&Editing. DCM: Conceptualization, Resources, Writing-Review&Editing, Supervision, Funding acquisition.

Conflicts of interest

The monomer, 2'-maleimideomethyl-3,4-ethylenedioxythiophene (EDOT-maleimide), is described as part of a US Patent (patent application number PCT/US2020/048495) submitted in 2020 by the University of Delaware. Beyond that we have no other conflicts of interest to disclose.

Acknowledgements

This research was supported by the National Science Foundation (DMR-1808048), the Air Force Office of Scientific Research MSIT Program for Next Generation Nanosystems, and the University of Delaware. We would like to thank the faculty and staff here at the University of Delaware including Wenbo Wu for help doing XPS, the Advanced Materials Characterization Lab for use of their GIWAXS, the W. M. Keck Center for Advanced Microscopy and Microanalysis for use of their SEM, and the Bio-imaging Center of the Delaware Biotechnology institute for use of their AFM (Delaware INBRE grant #P20 GM103446).

Notes and references

1 G. Wang, L. Zhang and J. Zhang, Chem. Soc. Rev., 2012, 41, 797–828.
2 Z. Wu, L. Li, J. Yan and X. Zhang, Advanced Science, 2017, 4, 1600382.
3 Z. Yang, J. Zhang, M. C. Kintner-Meyer, X. Lu, D. Choi, J. P. Lemmon and J. Liu, Chemical reviews, 2011, 111, 3577–3613.
4 J. Yeo, G. Kim, S. Hong, M. S. Kim, D. Kim, J. Lee, H. B. Lee, J. Kwon, Y. D. Suh, H. W. Kang, H. J. Sung, J.-H. Choi, W.-H. Hong, J. M. Ko, S.-H. Lee, S.-H. Choa and S. H. Ko, Journal of Power Sources, 2014, 246, 562–568.
5 B. K. Kim, S. Sy, A. Yu and J. Zhang, in Handbook of Clean Energy Systems, American Cancer Society, 2015, pp. 1–25.
6 B. E. Conway, J. Electrochem. Soc., 1991, 138, 1539.
7 A. Eftekhari, L. Li and Y. Yang, Journal of Power Sources, 2017, 347, 86–107.
8 A. Sardar and P. S. Gupta, AIP Conference Proceedings, 2018, 1953, 030020.
9 K. Sun, S. Zhang, P. Li, Y. Xia, X. Zhang, D. Du, F. H. Isikgor and J. Ouyang, J Mater Sci: Mater Electron, 2015, 26, 4438–4462.
10 M. J. Donahue, A. Sanchez-Sanchez, S. Inal, J. Qu, R. M. Owens, D. Mecerreyes, G. G. Malliaras and D. C. Martin, Materials Science and Engineering: R: Reports, 2020, 140, 100546.
11 A. Elschner, S. Kirchmeyer, W. Lovenich, U. Merker and K. Reuter, PEDOT: principles and applications of an intrinsically conductive polymer, CRC press, 2010.
12 J.-Y. Kim, M.-H. Kwon, Y.-K. Min, S. Kwon and D.-W. Ihm, Advanced Materials, 2007, 19, 3501–3506.
13 P. A. Levermore, R. Jin, X. Wang, L. Chen, D. D. C. Bradley and J. C. de Mello, Journal of Materials Chemistry, 2008, 18, 4414–4420.
14 Y. Soo Kim, S. Bin Oh, J. Hyeok Park, M. Suk Cho and Y. Lee, Solar Energy Materials and Solar Cells, 2010, 94, 471–477.
15 G. A. Snook and G. Z. Chen, Journal of Electroanalytical Chemistry, 2008, 612, 140–146.
16 H. Liu, W. Zhou, X. Ma, S. Chen, S. Ming, K. Lin, B. Lu and J. Xu, Electrochimica Acta, 2016, 220, 340–346.
17 L. Ouyang, C. Kuo, B. Farrell, S. Pathak, B. Wei, J. Qu and D. C. Martin, Journal of Materials Chemistry B, 2015, 3, 5010–5020.
18 M. Sterby, R. Emanuelsson, X. Huang, A. Gogoll, M. Strømme and M. Sjödin, Electrochimica Acta, 2017, 235, 356–364.
19 C. Karlsson, H. Huang, M. Strømme, A. Gogoll and M. Sjödin, RSC Adv., 2015, 5, 11309–11316.
20 H. Y. Du, X. X. Liu, Z. Ren and P. P. Liu, J Solid State Electrochem, 2018, 22, 3947–3954.
21 M. A. A. Mohd Abdah, N. A. Zubair, N. H. N. Azman and Y. Sulaiman, Materials Chemistry and Physics, 2017, 192, 161–169.
22 R. Vellacheri, H. Zhao, M. Mühlstädt, A. Al-Haddad, K. D. Jandt and Y. Lei, Advanced Functional Materials, 2017, 27, 1606696.
23 Y. Liu, I. Murtaza, A. Shuja and H. Meng, Chemical Engineering Journal, 2020, 379, 122326.
24 R. Liu, J. Duay, T. Lane and S. B. Lee, Phys. Chem. Chem. Phys., 2010, 12, 4309–4316.
25 P. Tang, L. Han, L. Zhang, S. Wang, W. Feng, G. Xu and L. Zhang, ChemElectroChem, 2015, 2, 949–957.
26 S. Lehtimäki, M. Suominen, P. Damlin, S. Tuukkanen, C. Kvarnström and D. Lupo, ACS Appl. Mater. Interfaces, 2015, 7, 22137–22147.
27 M. Tahir, L. He, W. A. Haider, W. Yang, X. Hong, Y. Guo, X. Pan, H. Tang, Y. Li and L. Mai, Nanoscale, 2019, 11, 7761–7770.
28 S. Y. Liew, W. Thielemans and D. A. Walsh, Journal of Solid State Electrochemistry, 2014, 18, 3307–3315.
29 J. Wang, Y. Xu, X. Chen and X. Du, Journal of Power Sources, 2007, 163, 1120–1125.
30 R. Liu, S. I. Cho and S. B. Lee, Nanotechnology, 2008, 19, 215710.
31 M. Rajesh, R. Manikandan, B. C. Kim, M. Becuwe, K. H. Yu and C. J. Raj, Electrochimica Acta, 2020, 354, 136669.
32 M. Sterby, R. Emanuelsson, F. Mamedov, M. Strømme and M. Sjödin, Electrochimica Acta, 2019, 308, 277–284.
33 S. Akoudad and J. Roncali, Electrochemistry Communications, 2000, 2, 72–76.
34 N. Bhagwat, K. L. Kiick and D. C. Martin, Journal of Materials Research, 2014, 29, 2835–2844.
35 E. C. Vermisoglou, P. Jakubec, A. Bakandritsos, M. Pykal, S. Talande, V. Kupka, R. Zbořil and M. Otyepka, Chem. Mater., 2019, 31, 4698–4709.
36 B. H. Northrop, S. H. Frayne and U. Choudhary, Polym. Chem., 2015, 6, 3415–3430.
37 R. G. Barradas, S. Fletcher and J. D. Porter, Journal of Electroanalytical Chemistry and Interfacial Electrochemistry, 1977, 75, 533–543.
38 S. Nagane, P. Sitarik, Y. Wu, Q. Baugh, S. Chhatre, J. Lee and D. C. Martin, MRS Advances, 2020, 5, 943–956.
39 V. Subramanian and D. C. Martin, Macromolecules, 2021, 54, 6956–6967.
40 S.-C. Luo, S. S. Liour and H. Yu, Chemical Communications, 2010, 46, 4731–4733.
41 C. O. Laoire, S. Mukerjee, K. M. Abraham, E. J. Plichta and M. A. Hendrickson, J. Phys. Chem. C, 2009, 113, 20127–20134.
42 S.-J. Xiao, M. Wieland and S. Brunner, Journal of Colloid and Interface Science, 2005, 290, 172–183.

43 M. P. Schwartz and R. J. Hamers, Surface Science, 2007, 601, 945–953.
44 L. Sheng, D. Fang, X. Wang, J. Tang, Q. Han, J. Zhou and W. Tang, Chemical Engineering Journal, 2020, 401, 126123.
45 B. Anothumakkool, R. Soni, S. N. Bhange and S. Kurungot, Energy Environ. Sci., 2015, 8, 1339–1347.
46 T. Atnafu Yemata, Y. Zheng, A. K. Ko Kyaw, X. Wang, J. Song, W. Shong Chin and J. Xu, RSC Advances, 2020, 10, 1786–1792.
47 S. T. Keene, T. P. A. van der Pol, D. Zakhidov, C. H. L. Weijtens, R. A. J. Janssen, A. Salleo and Y. van de Burgt, Advanced Materials, 2020, 32, 2000270.
48 D. Belaineh, J. W. Andreasen, J. Palisaitis, A. Malti, K. Håkansson, L. Wågberg, X. Crispin, I. Engquist and M. Berggren, ACS Appl. Polym. Mater., 2019, 1, 2342–2351.
49 C. M. Palumbiny, F. Liu, T. P. Russell, A. Hexemer, C. Wang and P. Müller-Buschbaum, Advanced Materials, 2015, 27, 3391–3397.
50 J. Zhang, S. Seyedin, S. Qin, P. A. Lynch, Z. Wang, W. Yang, X. Wang and J. M. Razal, Journal of Materials Chemistry A, 2019, 7, 6401–6410.
51 H. Topsoe, *Bulletin*, 1968, 472, 63.
52 S. Baek, R. A. Green and L. A. Poole-Warren, Journal of Biomedical Materials Research Part A, 2014, 102, 2743–2754.
53 J. Qu, L. Ouyang, C. Kuo and D. C. Martin, Acta biomaterialia, 2016, 31, 114–121.
54 H. Okuzaki and M. Ishihara, Macromolecular Rapid Communications, 2003, 24, 261–264.
55 R. Sarabia-Riquelme, M. Shahi, J. W. Brill and M. C. Weisenberger, ACS Appl. Polym. Mater., 2019, 1, 2157–2167.
56 X. Cui, J. F. Hetke, J. A. Wiler, D. J. Anderson and D. C. Martin, Sensors and Actuators A: Physical, 2001, 93, 8–18.
57 D. Raoufi, Physica B: Condensed Matter, 2010, 405, 451–455.
58 T. Silk, Q. Hong, J. Tamm and R. G. Compton, Synthetic Metals, 1998, 93, 65–71.
59 R. Gavrila, A. Dinescu and D. Mardare, Raman J Inf Sci Technol, 2007, 10, 291–300.
60 P. Simon, Y. Gogotsi and B. Dunn, Science, 2014, 343, 1210–1211.
61 Y. Gogotsi and R. M. Penner, ACS Nano, 2018, 12, 2081–2083.
62 Y. Xu, S. Pei, Y. Yan, L. Wang, G. Xu, S. Yarlagadda and T.-W. Chou, ACS Appl. Mater. Interfaces, 2021, 13, 11774–11782.
63 J. H. Shendkar, M. Zate, K. Tehare, V. V. Jadhav, R. S. Mane, M. Naushad, J. M. Yun and K. H. Kim, Materials Chemistry and Physics, 2016, 180, 226–236.
64 B. Pandit, S. S. Karade and B. R. Sankapal, ACS Appl. Mater. Interfaces, 2017, 9, 44880–44891.
65 B. Pandit, D. P. Dubal, P. Gómez-Romero, B. B. Kale and B. R. Sankapal, Scientific Reports, 2017, 7, 43430.
66 B. Pandit and B. R. Sankapal, New Journal of Chemistry, 2017, 41, 10808–10814.
67 N. Wang, G. Han, H. Song, Y. Xiao, Y. Li, Y. Zhang and H. Wang, Journal of Power Sources, 2018, 395, 228–236.
68 S. A. Ebrahim, M. E. Harb, M. M. Soliman and M. B. Tayel, Journal of Taibah University for Science, 2016, 10, 281–285.
69 R. Vicentini, L. M. Da Silva, E. P. Cecilio Junior, T. A. Alves, W. G. Nunes and H. Zanin, Molecules, 2019, 24, 1452.
70 J. Xiao, Q. Li, Y. Bi, M. Cai, B. Dunn, T. Glossmann, J. Liu, T. Osaka, R. Sugiura, B. Wu, J. Yang, J.-G. Zhang and M. S. Whittingham, Nature Energy, 2020, 5, 561–568.
71 J. J. Giner-Sanz, E. M. Ortega, M. García-Gabaldón and V. Pérez-Herranz, J. Electrochem. Soc., 2018, 165, E628.
72 K. R. Cooper and M. Smith, Journal of Power Sources, 2006, 160, 1088–1095.
73 M. Itagaki, S. Suzuki, I. Shitanda and K. Watanabe, Electrochemistry, 2007, 75, 649–655.
74 I. Yang, S.-G. Kim, S. H. Kwon, M.-S. Kim and J. C. Jung, Electrochimica Acta, 2017, 223, 21–30.
75 T. Q. Nguyen and C. Breitkopf, J. Electrochem. Soc., 2018, 165, E826.
76 P. L. Taberna, P. Simon and J. F. Fauvarque, J. Electrochem. Soc., 2003, 150, A292.
77 D. C. Martin, MRS Communications, 2015, 5, 131–152.
78 M. Bianchi, S. Carli, M. D. Lauro, M. Prato, M. Murgia, L. Fadiga and F. Biscarini, Journal of Materials Chemistry C, 2020, 8, 11252–11262.
79 A. M. Österholm, D. E. Shen, A. L. Dyer and J. R. Reynolds, ACS Appl. Mater. Interfaces, 2013, 5, 13432–13440.
80 Z. Wang, P. Tammela, J. Huo, P. Zhang, M. Strømme and L. Nyholm, J. Mater. Chem. A, 2016, 4, 1714–1722.
81 C. Decker and C. Bianchi, Polymer International, 2003, 52, 722–732.
82 J. Rivnay, P. Leleux, M. Ferro, M. Sessolo, A. Williamson, D. A. Koutsouras, D. Khodagholy, M. Ramuz, X. Strakosas and R. M. Owens, Science advances, 2015, 1, e1400251.